

1 **Can we use precipitation isotope outputs of Isotopic General Circulation Models to**
2 **improve hydrological modeling in large mountainous catchments on the Tibetan Plateau?**

3

4 Yi Nan¹, Zihua He², Fuqiang Tian¹, Zhongwang Wei³, Lide Tian⁴

5 ¹ Department of Hydraulic Engineering, State Key Laboratory of Hydrosience and Engineering,
6 Tsinghua University, Beijing 100084, China

7 ² Center for Hydrology, University of Saskatchewan, Saskatchewan, Canada

8 ³ Guangdong Province Key Laboratory for Climate Change and Natural Disaster Studies, School of
9 Atmospheric Sciences, Sun Yat-sen University, Guangzhou, Guangdong, China

10 ⁴ Institute of International Rivers and Eco-security, Yunnan University, Kunming, China

11 ***Corresponding to:*** Fuqiang Tian

12 Address: Room 330 New Hydraulic Building, Tsinghua University, Beijing 100084, China

13 Email: tianfq@mail.tsinghua.edu.cn

14 _____

15 Abstract

16 Issues related to large uncertainty and parameter equifinality have posed big challenges
17 for hydrological modeling in cold regions where runoff generation processes are particularly
18 ~~complex~~complicated. Tracer-aided hydrological models ~~that coupling-integrate modules to~~
19 ~~simulate the~~ transportation and fractionation processes of water stable isotope are increasingly
20 used to constrain parameter uncertainty and refine the parameterizations of specific
21 hydrological processes in cold regions. However, commonly unavailability of site sampling of
22 ~~spatially distributed~~spatially distributed precipitation isotope hampers the practical
23 applications of tracer-aided models in large scale catchments. This study, taken the precipitation
24 isotope data (isoGSM) derived from the Isotopic General Circulation Models (iGCM) as an
25 example, explored its utility in driving a tracer-aided hydrological model in the Yarlung
26 Tsangpo River basin (YTR, around 2×10^5 km² with mean elevation of 4875 m) on the Tibetan
27 Plateau (TP). The isoGSM product was firstly corrected based on the biases between gridded
28 precipitation isotope estimates and limited site sampling measurements. Model simulations
29 driven by the corrected isoGSM data were then compared with those forced by spatially
30 interpolated precipitation isotope from site sampling measurements. Our results indicated that:
31 (1) spatial precipitation isotope derived from the isoGSM data helped to reduce modeling
32 uncertainty and improve parameter identifiability in a large mountainous catchment on the TP,
33 in comparison to a calibration method using discharge and snow cover area fraction without
34 any information of water isotope; (2) model parameters estimated by the corrected isoGSM
35 data presented higher transferability to nested sub-basins and produced higher model
36 performance in the validation period than that estimated by the interpolated precipitation
37 isotope data from site sampling measurements; (3) model calibration ~~procedure~~ forced by the
38 corrected isoGSM data successfully rejected parameter sets that overestimated glacier melt
39 contribution and gave more reliable contributions of runoff components, indicating the
40 corrected isoGSM data served as a better choice to provide informative spatial precipitation
41 isotope than the interpolated data from site sampling measurements at macro scale. This work
42 suggested plausible utility of combining isoGSM data with measurements even from a sparse
43 sampling network in improving hydrological modeling in large ~~mountain~~high mountainous
44 ~~catchments~~basins.

45 Key word

46 Tracer-aided hydrological modeling; Large basins on the Tibetan Plateau; Isotopic General
47 Circulation Models (iGCM) product; Combining isoGSM isotope data with measurements at
48 sparse sampling sitesiGCM correction with sparse measurements.

49

50 1. Introduction

51 Large uncertainty and strong equifinality of parameter calibration are the widely ~~faeed~~
52 recognized issues in hydrological modelling (Gupta et al., 2008), especially in cold regions
53 where hydrological complexity is highly enhanced by the competitions of multiple water inputs
54 and the strong spatio-temporal variabilities of runoff generation processes (Zongxing-Li et al.,
55 2019). ~~-~~Tracer-aided hydrological models integrating a water or environmental tracer (e.g.,
56 stable oxygen isotope, $\delta^{18}\text{O}$) module into the runoff generation architecture have been proved
57 as highly valuable in improving parameter calibration and diagnosing model uncertainty (Son
58 and Sivapalan, 2007; Birkel et al., 2011; Capell et al., 2012; He et al., 2019). Multiple-objective
59 calibration of tracer-aided model towards both runoff and isotope simulation allows for
60 rejection of parameters based on runoff observation alone, consequently makes the model
61 satisfy multiple objectives and reduces the model uncertainty (McGuire et al., 2007). However,
62 practical applications of tracer-aided hydrological modeling are mainly limited in only small to
63 meso scales. The largest basin area where previous tracer-aided modelling ~~works have has~~ been
64 ~~successfully~~ implemented is around 10^3 km^2 (e.g., Delavau et al., 2017; Campell et al., 2012;
65 Stadnyk et al., 2013). Reasons fall in either the lumped conceptual model structures due to the
66 complicated ~~ex~~ tracer processes difficult to be coupled with distributed model (Birkel and
67 Soulsby, 2015), ~~which are particularly not suitable for capturing the strong spatial variability of~~
68 ~~hydrological behaviors in large scale basins~~, or the low availability of tracer data in large basins
69 due to difficulties in the long-term, continuous and high-frequency field sampling works (e.g.,
70 Ala-aho et al., 2017; He et al., 2019). The structure and data issues make the model not suitable
71 for capturing the strong spatial variability of hydrological behaviors in large scale basins.

72 The Tibetan Plateau (TP) is the source region of ~~several~~ many large rivers (e.g.,
73 Brahmaputra, Ganges, Indus, Mekong, among others), which sustain the ecosystems and
74 provide a great proportion of water source for downstream livelihoods and agricultural
75 irrigation (Zhang et al., 2013; Schaner et al., 2012). Decision making of water resource
76 management over TP and its downstream area relies heavily on river runoff in the large basins.
77 Meanwhile, melting water from snow and ice contributes a large significant proportion to river
78 runoff in the large basins on TP due to the cold climate and glacier coverage in head watersheds
79 (Zongxing-Li et al., 2019). Runoff in this region is thus highly vulnerable to climate warming.
80 Robust quantification of the contribution of meltwater to river runoff is critical in understanding
81 water resources dynamics on TP (Immerzeel et al., 2013). Although great efforts have been
82 ~~taken~~ conducted to quantify the contributions of runoff components (e.g., Immerzeel et al., 2010;
83 Lutz et al., 2014) and their future trends under climate changes on TP (e.g., Immerzeel et al.,
84 2010; Lutz et al., 2014; Su et al., 2016; Masood et al., 2015), results reported in the wide range

85 of studies show substantial differences (Xu et al., 2019; Tian et al., 2020). The disagreement
86 among studies ~~which~~ indicates big challenges on quantifying contributions of runoff
87 components and predicting their future trend in the large basins on TP. The difficulty of this
88 task is mainly related to the large uncertainty of hydrological modelling and parameter
89 calibration in the TP, because of the complex hydrological processes (He et al., 2018) and the
90 commonly inaccurate estimation of precipitation (Xu et al., 2017; He et al. 2017). The strong
91 inter-competitions of runoff processes induced by meltwater ~~and~~ versus rainwater and surface
92 water versus subsurface water were inadequately constrained in hydrological models by the
93 commonly used hydrological observation of streamflow (Duethmann et al., 2015),- and even
94 additional data of snow/ice coverage (He et al. 2019) ~~which further enhanced the equifinality~~
95 ~~issue of parameter identification in large basins on TP~~. Reducing the modelling uncertainty
96 originated from parameter calibration is essential for proper understanding of runoff regimes
97 and robust prediction of future hydrological change.

98
99 Tracer-aided hydrological models that additionally involved water stable isotope data for
100 parameter calibration have been proved as highly capable on constraining the inter-
101 competitions of runoff processes induced by meltwater and rainwater in high mountains (He et
102 al. 2019; Nan et al. 2021), which, however, have not been tested in large basins yet due to the
103 unavailability of precipitation isotope data. Global gridded isotope product potentially serves
104 as an alternative forcing of precipitation isotope data for tracer-aided hydrological models in
105 large basins where high-frequency sampling work in a large region is not feasible. One of these
106 options comes to outputs of the isotopic General or Regional Circulation Models (iGCM and
107 iRCM, Noone and Sturm, 2010; Xi, 2014; Sturm et al., 2005, 2007), which has been proved to
108 have high performance on simulating the seasonal and spatial variations of isotopic signature
109 of precipitation on regional and global scales (Wang et al., 2017; Yao et al., 2013). However,
110 very few works have been conducted to test the behavior of such products on forcing
111 hydrological models. To the best of our knowledge, the only one work was conducted by
112 Delavau et al. (2017), who examined the performance of an iRCM product REMOiso on forcing
113 tracer-aided model in a regional catchment of around 10^3 km² in Canada. Their results indicated
114 that hydrological simulations driven by the iRCM product reproduced the variations of isotopic
115 signature ($\delta^{18}\text{O}$) of river water comparably to the simulations driven by $\delta^{18}\text{O}$ measurements
116 from sampling sites and improved the representations of internal hydrological processes in the
117 model. Those attempts provide sound confidences for exploring the utility of global and
118 regional gridded isotope data products in aiding hydrological modeling in large basins on TP.

119 Motivated by the mentioned backgrounds, we adopted a tracer-aided hydrological model
120 developed by Nan et al. (2021) to simulate runoff processes and the contributions of runoff
121 components to streamflow in a large basin extending around 2×10^5 km² on the TP. The isotope

122 module was driven by two kinds of precipitation isotope data including site measurements from
123 water samples and outputs of iGCM. Scientific questions addressed in this study are two-fold:
124 (1) what are the benefits of involving water isotope data for hydrological modeling in larger
125 catchments? (2) how does the gridded precipitation isotope data of iGCM products perform on
126 forcing tracer-aided hydrological model in large basins?

127 **2. Materials and methodology**

128 **2.1 Study area**

129 The Yarlung Tsangpo River (YTR) located in the southern TP on the north of Himalaya
130 Mountain (Fig. 1) is one of the longest rivers (longer than 2000 km) originating from TP. The
131 YTR basin is located in the range of 27-32°N and 82-97°E, with an elevation range of 2900-
132 6900 m a. s. l. The mean annual precipitation in YTR basin is around 470 mm, which is
133 dominated by South Asian Monsoon in the Indian Ocean hydrosphere-atmosphere system,
134 resulting in obvious wet season from June to September (Dong et al., 2016). Contributing area
135 to the Nuxia hydrological station extends approximately 2×10^5 km², around 2% of which is
136 covered by glacier. Plenty of previous works have shown the great contribution of snow and
137 glacier melting to the runoff in YTR (e.g., Chen et al., 2017; Tian et al., 2020).

138 The Karuxung River (KR) catchment is located in the upper region of YTR basin, on the
139 northern slope of the Himalayan Mountains, which is used for model evaluation in sub-basin
140 because of its high glacierized area proportion (around 20%). The KR originates from the Lejin
141 Jangsan Peak of the Karola Mountain at 7206 m above sea level (a.s.l.), and flows into the
142 Yamdrok Lake at 4550m a.s.l. (Zhang et al., 2006a). The KR catchment covers an area of 286
143 km². Runoff in KR catchment is strongly influenced by the headwater glaciers which cover an
144 area of around 58 km².

145 **[Figure 1]**

146 **2.2 Hydro-meteorological data and site water sampling for isotope analysis**

147 Digital elevation model (DEM) data in the YTR catchment with a spatial resolution of 30-
148 m was extracted from the Geospatial Data Cloud (<http://www.gscloud.cn>). The 3-hour $0.1^\circ \times 0.1^\circ$
149 China Meteorological Forcing Dataset (CMFD) which combined multiple datasets (e.g.,
150 GLDAS and TRMM) with the national meteorological station data (Yang et al., 2010) provided
151 meteorological inputs including precipitation, temperature and potential evapotranspiration.
152 Glacier coverages were extracted from the Second Glacier Inventory Dataset of China (Liu,
153 2012). The Tibetan Plateau Snow Cover Extent product (TPSCE, 5km×5km, Chen et al., 2018)
154 were used to denote the fluctuations of daily snow cover area (SCA) in the basins, which also
155 included the glacier cover area. The 8-day Leaf Area Index (LAI) and the monthly normalized
156 difference vegetation index (NDVI) data were downloaded from MODIS products of

157 MOD15A2H (500m×500m, [Myneni et al., 2015](#)) and MOD13A3 (1km×1km, [Didan, 2015](#)),
158 respectively. Soil parameters were estimated based on the soil properties extracted from the
159 1km × 1km Harmonized World Soil Database (HWSD, <http://www.fao.org/geonetwork>).

160 Daily streamflow during 2000-2010 for hydrological calibration were observed at the
161 Nuxia, Yangcun and Nugesha hydrological stations. Grab samples of precipitation and stream
162 water were collected in 2005 at four stations along the main stream of YTR, i.e., Lazi (4889 m
163 a.s.l.), Nugesha (4715 m a.s.l.), Yangcun (4541 m a.s.l.) and Nuxia (3691 m a.s.l.), from the
164 upstream to the downstream (Fig. 1). Precipitation water were sampled as immediately as
165 possible after the precipitation events, and stream water samples were collected weekly every
166 Monday from the river. [Considering the continental effect and elevation effect on precipitation
167 isotope, Considering the west-east flowing direction of the river \(Fig. 1b\) and the effect of
168 altitude,](#) the measured isotopic composition of precipitation from site sampling was
169 interpolated by longitude and altitude (similar with [Zhao et al. 2012](#), [Liu et al. 2014](#)) using Eq.
170 1 to provide spatial precipitation isotope for model input, in which the coefficients x , y and z
171 were estimated by least squares fitting the average precipitation $\delta^{18}\text{O}$ and corresponding
172 altitude/longitude at the four measuring stations. [The coefficient \$x\$ reflected the altitudinal lapse
173 of precipitation isotope, thus was expected to be lower than \$\theta\$ zero. Longitude reflected the
174 distance from the station to the mainland border, thus the coefficient \$y\$ was expected to be larger
175 than 0. The term latitude was not chosen as a regression variable, because of the similar latitude
176 of the measurement stations and the relatively narrow north-south range of the basin \(Fig. 1\).](#)
177 Isotopic composition of glacier meltwater was assumed to be constant during the entire study
178 period, and lower than the amount weighted average isotopic composition of precipitation.

179
$$\overline{\delta^{18}\text{O}_{precipitation}}(\text{‰}) = x * ALT(m) + y * LON(^{\circ}E) + z \quad (1)$$

180 Daily temperature and precipitation in the KR catchment during 2006-2012 were collected
181 at the Langkazi meteorological Station. Altitudinal distributions of temperature and
182 precipitation across the catchment were estimated by the lapse rates reported in [Zhang et al.
183 \(2015\)](#). Daily streamflow during 2006-2012 for hydrological calibration and evaluation were
184 measured at the Wengguo hydrological station. Grab samples of precipitation and stream water
185 at the Wengguo Station in 2006-2007 and 2010-2012 were collected for isotope analysis.
186 Isotopic composition of precipitation over elevation bands was calculated from the sampling
187 site of Wengguo Station using an altitudinal lapse of -0.34‰/100m reported in [Liu et al. \(2007\)](#).
188 Isotopic composition of glacier meltwater in this catchment was assumed to be -18.9‰,
189 constantly throughout the entire study period, adopting from the value reported in [Gao et al.
190 \(2009\)](#). Details of water samples in YTR and KR catchments are summarized in Table 1.

191 **[Table 1]**

2.3 Isotopic General Circulation Model isoGSM and bias correction

Precipitation $\delta^{18}\text{O}$ of the Scripps global spectral model with water isotopes-incorporated (isoGSM) developed by Yoshimura et al. (2008) was extracted to drive the tracer-aided model. IsoGSM was developed from the Scripps Experimental Climate Prediction Center's GSM, which was based on the medium range forecast model for making operational analysis and predictions (Kanamitsu et al., 2002). Wang et al. (2017) evaluated the performance of ten iGCM datasets in five aspects of average isotope simulation, seasonal difference, temperature effect, precipitation effect and the global meteoric water line, ranking isoGSM as 1, 2, 1, 2 and 2 respectively, indicating a relatively best performance of isoGSM among the iGCMs. According to a previous comparison of ten iGCMs in Wang et al. (2017), the isoGSM product showed the best performance on simulating global spatial pattern of precipitation $\delta^{18}\text{O}$. The spatial and temporal resolutions of isoGSM dataset are $1.875^\circ \times 1.875^\circ$ and 6 hours, respectively.

The precipitation $\delta^{18}\text{O}$ estimated by isoGSM was corrected by site sampling measurements in Eqs. 2-4 before being used for hydrological model input. Biases between the amount weighted averages of isoGSM isotope and sampling measurement at the four sampling sites in YTR basin were calculated in Eq. 2 first. Spatial distribution of bias between isoGSM isotope and sampling measurement was then assumed as linearly related to altitude in Eq. 3, in which the coefficients of a and b were estimated by least squares fitting the site biases calculated in Eq. 2 and corresponding site altitudes. Daily isoGSM isotope data in hydrological model units over the study catchment were finally corrected in Eq. 4 using the unit altitudes.

$$bias_i = \overline{\delta^{18}O_{i,m}} - \overline{\delta^{18}O_{i,G}} \quad i = 1,2,3,4 \quad (2)$$

$$bias_r = a * ALT + b \quad (3)$$

$$\begin{cases} bias_{r_k} = \delta^{18}O_{k,j,G} + a * ALT_k + b \\ \delta^{18}O_{k,j,Corr} = \delta^{18}O_{k,j,G} + bias_r \end{cases} \quad (4)$$

where, $\overline{\delta^{18}O_{i,m}}$ is the amount weighted average of measured precipitation isotope over the sampling period in sampling site i ($i=1-4$), and $\overline{\delta^{18}O_{i,G}}$ is the amount weighted average of isoGSM precipitation isotope over the study period in pixel that contains the sampling site i . ALT is altitude of the sampling site or hydrological model unit. Parameters a and b are the linear regression coefficients. $\delta^{18}O_{ki,j,Corr}$ and $\delta^{18}O_{ki,j,G}$ are the corrected and original isoGSM precipitation isotope at all the hydrological model unit ki ($ki=1-63$) on the j^{th} day, respectively. Performance of the correction method of isoGSM data was evaluated by sampling measurement of precipitation isotope at the Wengguo station in the KR sub-basin, which was not involved in the estimation of coefficients a and b in Eq. 3. Spatial precipitation isotope of the isoGSM data in the KR sub-basin for hydrological modeling was estimated using the same altitudinal lapse that was used to interpolate the sampling data in Section 2.2, because the KR catchment only

226 encompasses one pixel of the isoGSM data.

227 **2.4 Tracer-aided hydrological model**

228 A distributed tracer-aided hydrological model THREW-t (Tian et al., 2006; Nan et al., 2021)
229 was adopted in this study for streamflow and isotope simulations. This model uses the
230 Representative Elementary Watershed (REW) method for the spatial discretization of
231 catchment, in which the study catchment is first divided into REWs based on the catchment
232 DEM. Each REW is further divided into two vertical distributed layers (surface and subsurface
233 layers), including eight hydrological sub-zones according to using land covers and soil
234 properties within the REW. Hydrological processes including canopy interception, infiltration,
235 infiltration-excess runoff, saturation-excess runoff and groundwater outflow were simulated in
236 each REW. REW is based on the self-similar characteristics of a watershed and its sub-
237 watersheds (Reggiani et al., 1999), and is regarded as the fundamental component of
238 hydrological processes and modelling, in which series of balance equations are established. The
239 principle of REW division is based on the scale of interest, modelling purpose, and the data
240 availability (Tian et al., 2006, 2008). In total, 63 and 41 REWs were extracted in YTR and KR,
241 respectively, which were adopted in two previous studies (Tian et al., 2020; Nan et al., 2021).
242 Areal averages of the gridded estimates of CMFD meteorological variables and precipitation
243 $\delta^{18}\text{O}$ were used in each of the REWs to drive the hydrological model. For application in cold
244 and high regions, a module representing the glacier melting and snowpack evolution was
245 incorporated into the original model in Tian et al. (2006), which has been proved as successful
246 in previous modelling works (e.g., He et al., 2015; Xu et al., 2019; Tian et al., 2020). The semi-
247 distributed REW-based structure made the model concise enough to couple the tracer module
248 easily. The tracer module was developed by Nan et al. (2021) which performed quite well on
249 reproducing the isotopic signature of stream water in the KR catchment. The isotope mixing
250 and fractionation processes were simulated based on the completely mixing assumption and the
251 Rayleigh fractionation method (Hindshaw et al., 2011; Wolfe et al., 2007). Forced by the input
252 data of precipitation isotope composition, the model can simulate the isotopic evolution all the
253 water bodies in the watershed, including soil water, snowpack, stream water, etc. The THREW-
254 t model considered the runoff components to stream water based on two aspects (Nan et al.,
255 2021). First is based on the individual water sources in the total water input forcing runoff
256 processes including rainfall, snowmelt and glacier melt. Second is based on the runoff-
257 generation processes including surface runoff and subsurface runoff (baseflow). The THREW-
258 t model mainly described the rainfall-runoff processes, thus only the role of shallow
259 groundwater which can be recharged by the rainfall was considered, but the contribution from
260 deep groundwater storage was not simulated. More details of model description and set up are
261 given in Tian et al. (2006) and Nan et al. (2021).

262

263 The physical basis and value ranges of the calibrated parameters in the THREW-t model
264 are described in Table 2. In both modeling catchments of YTR and KR, the parameter values
265 were optimized using three calibration variants: (1) a dual-objective calibration using observed
266 discharge and MODIS snow covered area fraction (SCA), (2) a triple-objective calibration
267 using observed discharge, MODIS SCA and $\delta^{18}\text{O}$ measurements of stream water forced by
268 linearly interpolated measurements of site sampling precipitation isotope, and (3) a triple-
269 objective calibration using observed discharge, MODIS SCA and $\delta^{18}\text{O}$ measurements of stream
270 water but forced by the isoGSM precipitation isotope data. Metrics used to evaluate the
271 simulations of discharge, SCA and isotope are list in Eqs. 5-7.

$$272 \quad NSE_{dis} = 1 - \frac{\sum_{i=1}^n (Q_{o,i} - Q_{s,i})^2}{\sum_{i=1}^n (Q_{o,i} - \overline{Q_o})^2} \quad (5)$$

$$273 \quad RMSE_{SCA} = \sqrt{\frac{\sum_{i=1}^n (SCA_{o,i} - SCA_{s,i})^2}{n}} \quad (6)$$

$$274 \quad MAE_{iso} = \frac{\sum_{i=1}^n |\delta^{18}\text{O}_{o,i} - \delta^{18}\text{O}_{s,i}|}{n} \quad (7)$$

275 where, n is the total number of observations. Subscripts of o and s refer to observed and
276 simulated variables, respectively. $\overline{Q_o}$ is the average value of observed streamflow during the
277 assessing period.

278 [Table 2]

279 An automatic procedure based on the pySOT optimization algorithm developed by
280 Eriksson et al. (2015) was implemented for all the three calibration variants to identify the
281 behavioral parameters. The pySOT used surrogate model to guide the search for improved
282 solutions, with the advantage of needing few function evaluations to find a good solution. An
283 event-driven framework POAP were used for building and combining asynchronous
284 optimization strategies. The optimization was stopped if a maximum number of allowed
285 function evaluations was reached, which was set as 3000 in this study. For both modeling
286 catchments, the pySOT algorithm was repeated 150 times for each calibration variant. Although
287 the measurement unit of NSE_{dis} is different from $RMSE_{SCA}$ and MAE_{iso} , their values are in the
288 same order of magnitude (0-1) when the model performances were acceptable (Ala-aho et al.,
289 2017; Nan et al., 2021). Consequently, they were combined with equal weights for
290 simplification to represent the simultaneous performance on multiple objectives. For the
291 dual- and triple-objective calibration variants, $NSE_{dis} - RMSE_{SCA}$, $NSE_{dis} - RMSE_{SCA} - MAE_{iso}$
292 were chosen as combined optimization objectives, respectively. Among the 150 final parameter
293 sets produced by the pySOT runs, the behavioral parameter sets were selected by NSE_{dis}
294 thresholds, i.e., only the parameter sets producing NSE_{dis} higher than an assumed threshold were
295 regarded as behavioral parameter sets. Considering the model behaviors in the two catchments,
296 the NSE_{dis} threshold was chosen as 0.85 for the YTR basin, and was chosen as 0.75 and 0.70

297 [for dual- and triple-objective calibration variants in KR catchment, respectively. Focusing on](#)
298 [the utility of isoGSM on forcing tracer-aided model, the influence of calibration objective](#)
299 [function and weight of each objective were not assessed in this study.](#)

300 ~~For the YTR catchment, the NSE_{dis} threshold was chosen as 0.85. For KR catchment, the~~
301 ~~threshold was chosen as 0.75 and 0.70 for dual and triple objective calibration variants,~~
302 ~~respectively.~~

303 Considering the data availability, the calibration and validation periods for KR catchment
304 were set as 2006-2010 and 2011-2012, respectively. For YTR basin, discharge measured at the
305 outlet station Nuxia, the MODIS SCA fraction over the basin area upper the Nuxia station, and
306 the stream water $\delta^{18}O$ measured at the Nuxia station were used for calibration. Calibration and
307 validation periods of 2001-2005 and 2006-2010 were selected to test the model performance
308 for simulations of discharge and SCA at the Nuxia station. In addition, discharge measured at
309 the internal hydrological stations of Yangcun and Nugesha during 2001-2010 were used to
310 validate the spatial consistency of the calibrated model parameters. Model performance on
311 simulating stream water isotope at the Nuxia station in a validation period was not assessed as
312 stream water isotope measurements were available only during 2005. However, stream water
313 $\delta^{18}O$ measured during 2005 at the internal hydrological stations of Yangcun, Nugesha and Lazi
314 were adopted to validate the model performance on simulating spatial stream water $\delta^{18}O$ within
315 YTR basin.

316 **3. Results**

317 **3.1 Comparison between isoGSM and measured precipitation $\delta^{18}O$**

318 Figs. 2a and 3a show the comparison between isoGSM and measured precipitation $\delta^{18}O$ at
319 four sampling sites in the YTR basin. The isoGSM data presented similar fluctuations of
320 seasonal precipitation $\delta^{18}O$ to the sampling measurements (Fig. 3a). In particular, both isoGSM
321 and sampling measurement showed high precipitation $\delta^{18}O$ in May, and reached relatively low
322 values in the wet season during August and September. However, the original isoGSM data
323 tended to overestimate the measured precipitation $\delta^{18}O$ in the sampling periods (Fig. 2a). From
324 downstream to upstream, the amount weighted average precipitation $\delta^{18}O$ of samples collected
325 at the four stations (Nuxia, Yangcun, Nugesha and Lazi) were -9.58‰, -14.01‰, -14.80‰ and
326 -17.86‰, respectively, while the corresponding weighted average values of isoGSM pixels
327 containing the sampling stations during the same period were -7.53‰, -8.38‰, -9.22‰ and -
328 9.61‰, respectively. Bias between isoGSM data and sampling measurement tended to be larger
329 at upstream stations with higher elevations, partly due to the coarse spatial resolution of GCM
330 which cannot reproduce the effect of regional topography well. In contrast, the corrected
331 isoGSM data (black lines in Fig. 3a) captured the relatively low values in the late wet season

332 better than the original data (grey lines in Fig. 3a), and the scatter points fall closer to the 1:1
333 line (Fig. 2b). The MAE of isoGSM precipitation $\delta^{18}\text{O}$ in the YTR reduced from 6.65‰ to 4.91‰
334 after correction. Similarly, the original isoGSM data presented comparable seasonal
335 fluctuations of precipitation isotope to the sampling measurement at the Wengguo station in the
336 KR catchment (Fig. 3b), but the amount weighted average of precipitation $\delta^{18}\text{O}$ in the original
337 isoGSM data (-10.95‰) is much higher than that in the sampling measurement (-15.97‰, Fig.
338 2c and 3b). After bias correction, the overestimation was much reduced (Fig. 2d), indicated by
339 a reduced MAE value from 6.24‰ to 4.47‰. Underestimation of precipitation $\delta^{18}\text{O}$ by the
340 original isoGSM data in springs of 2011 and 2012, however, was not improved by the bias
341 correction.

342 **[Figure 2]**

343 **[Figure 3]**

344 Based on the multiple linear regression, the coefficients x , y and z in Eq. 1 were estimated
345 as -0.003, 0.574 and -52.6, respectively, with a R^2 value of 0.98, to interpolate the measured
346 isotope data to estimate spatial precipitation isotope over the YTR basin. The negative x and
347 positive y values were consistent with their physical meanings. Parameters a and b in Eq. 3
348 were estimated as -0.0046 and 14.96 based on the biases between isoGSM data and sampling
349 measurements on the four sampling sites in YTR. Fig. 4 and Fig. 5 shows the comparison of the
350 amount weighted averages of precipitation $\delta^{18}\text{O}$ on 63 REWs derived from the corrected
351 isoGSM data and interpolated sampling measurement. It is shown that the distributions of
352 precipitation isotope with altitude were rather similar in the two datasets (Fig. 4b). However,
353 distributions across the longitudes show visible differences ~~(Fig. 4a)~~. The largest differences
354 between the two datasets were located in the west upstream region (longitude $< 86^\circ$) and the
355 source region of tributary Lhasa River ($93^\circ > \text{longitude} > 86^\circ$, latitude $> 30^\circ$) (Fig. 4a and 5).
356 In comparison to the corrected isoGSM data, the interpolated sampling measurement estimated
357 much lower isotope signature in the ~~west-upstream region (longitude $< 86^\circ$)~~, while presenting
358 higher ~~the~~ isotope signature in the ~~east-middle and downstream regions~~ upper Lhasa River
359 (longitude falls between 91° and 93°). As site sampling data of precipitation was insufficient to
360 test which of the two datasets captured the west-east distribution of precipitation isotope better,
361 model performance on simulating isotope signatures of stream water measured at hydrological
362 stations from west to east forced by the two datasets provide a perspective to assess the
363 precipitation isotope estimations.

364 **[Figure 4]**

365 **[Figure 5]**

366 **3.2 Model performance for the simulations of discharge and stream water isotope**

367 Fig. 6-7 and Table 3 show the model performance of different calibration variants in the

368 YTR basin produced by the behavioral parameter sets. The three calibration variants produced
369 similar simulations of discharge and SCA (Fig. 6), in spite of the slightly higher NSE_{dis} and
370 lower $RMSE_{SCA}$ estimated by the dual-objective calibration (Table 3). For the simulation of
371 stream water $\delta^{18}O$, the dual-objective calibration produced the worst MAE_{iso} values in three out
372 of the four testing stations with the largest uncertainty ranges (Fig. 7a), which can be expected
373 as isotope data was not involved in this calibration. The two triple-objective calibration variants
374 produced good simulation for the stream water isotope at the Nuxia station in the calibration
375 year of 2005 (Fig. 7b and 7c). However, the triple-objective calibration variant forced by
376 isoGSM data estimated worse performance (i.e., higher MAE_{iso} values) for stream water $\delta^{18}O$
377 at the stations of Yangcun and Nugesha than the calibration forced by interpolated sampling
378 measurement showing significant underestimations for peak isotope values in June at Yangcun
379 station, and higher overestimations for isotope values after August at Nugesha. This was due to
380 the poor performance of isoGSM on capturing the isotope signature of individual precipitation
381 events during a specific period (see Fig. 3a), although being corrected already. For example,
382 the amount weighted average of measured precipitation $\delta^{18}O$ in June at the Yangcun station was
383 -5.87% , while the average of corrected isoGSM data showed a value of -10.09% , leading to
384 an underestimated peak value. Similarly, the amount weighted average of measured
385 precipitation $\delta^{18}O$ at Nugesha during August was -16.34% , while the corrected isoGSM data
386 estimated an average of -11.47% , leading to an overestimated stream $\delta^{18}O$ in the late wet season.
387 In spite of that, the performance of simulated stream water $\delta^{18}O$ at Nuxia, Yangcun and Nugesha
388 stations forced by corrected isoGSM data can still be considered as acceptable, given the
389 MAE_{iso} values were generally around 1 (Fig. 7c). For the most upstream station Lazi, however,
390 the triple-objective variant forced by measured precipitation $\delta^{18}O$ produced significantly
391 underestimated $\delta^{18}O$ of stream water, likely due to the underestimated precipitation $\delta^{18}O$ in the
392 upstream high altitudes produced by the interpolated measurement data (Fig. 4a**b** and 5). The
393 good performance of simulated stream water $\delta^{18}O$ at the Lazi station driven by the corrected
394 isoGSM data demonstrated that the corrected isoGSM estimated a better precipitation isoscape
395 in high altitudes of the study catchment than the linearly interpolated measurement data, partly
396 benefiting from the information of spatial precipitation isotope implied in the gridded values.
397 It is worth noting that the model simulations forced by corrected isoGSM estimated narrower
398 uncertainty bands for stream water $\delta^{18}O$ at Nuxia, Yangcun and Nugesha, and smaller value
399 ranges of the MAE_{iso} metric at all the four stations, in comparison to the simulations driven by
400 the interpolated precipitation $\delta^{18}O$. Compared to the simulations yielded by the dual-objective
401 calibration, the triple-objective calibration variants simulated smaller uncertainty ranges for
402 stream water $\delta^{18}O$ and slightly narrowed value ranges of objective metrics for the simulations
403 of discharge and SCA with the lower behavioral ratios of calibrated parameter sets in Table 3,
404 indicating good potential of isotope data on reducing modeling uncertainty and improving

405 parameter identifiability.

406 **[Figure 6]**

407 **[Figure 7]**

408 **[Table 3]**

409 The simulated hydrographs at two internal hydrological stations of Yangcun and Nugesha
410 were compared in Fig. 8 to assess the spatial consistency of model parameters calibrated by the
411 different variants. The isoGSM-forced triple-objective calibration produced the highest
412 performance for discharge simulation at the two internal stations (Fig. 8e and 8f) indicated by
413 the highest averages (0.82 and 0.74 for Yangcun and Nugesha) and minimal values (0.72 and
414 0.53 for Yangcun and Nugesha) of NSE, as well as the smallest values ranges of NSE. The dual-
415 objective calibration produced lower performance for discharge simulation than the isoGSM-
416 forced triple-objective calibration (with average NSE as 0.8 and 0.67 at Yangcun and Nugesha)
417 with a much larger uncertainty of the baseflow simulation (Fig. 8a and Fig. 8b). The
418 [measurementinterpolation](#)-forced triple-objective calibration produced higher mean NSE (0.81
419 and 0.74 for Yangcun and Nugesha) but smaller minimal NSE (0.62 and 0.31 for Yangcun and
420 Nugesha) than the dual-objective calibration with the largest values ranges of NSE at the two
421 stations. Moreover, the isoGSM-forced triple-objective calibration performed best on capturing
422 the peak flows in summer at both stations.

423 **[Figure 8]**

424 The model performances produced by the behavioral parameter sets of different calibration
425 variants in the KR catchment were shown in Figs. 9-10 and Table 4. All the three calibration
426 variants presented similar performances on simulating streamflow, while the two triple-
427 objective calibrations resulted in narrower uncertainty ranges, especially for the baseflow (Fig.
428 9c and e). The declining SCA in spring-summer was captured well in all the calibration variants
429 (Figs. 9b, d and f). Triple-objective calibrations driven by the two isotope datasets performed
430 comparably well on simulating the isotopic composition of stream water in the calibration
431 period (Fig. 10b and 10c) indicated by the low average values of MAE_{iso} (0.68 and 0.69) and
432 the well captured seasonal fluctuations of stream water $\delta^{18}O$. The peak isotopic values in around
433 June of 2007 were not captured well by the isoGSM-driven model (Fig. 10c), resulting in a
434 relatively larger minimal MAE_{iso} (0.57) than the interpolated measurement-driven result (0.48).
435 This was due to the underestimations of isoGSM on estimating the isotope signatures of
436 individual extreme precipitation events in June (see Fig. 3b). Specifically, there was a
437 precipitation event larger than 20mm/day in June of 2007, of which the corrected isoGSM
438 produced significantly lower $\delta^{18}O$ (-21.55‰) than the sampling measurement (-9.83‰) at the
439 Wengguo station. Despite that, the isoGSM-forced triple-objective calibration estimated much
440 better performance than the interpolated measurement-driven calibration for stream water $\delta^{18}O$
441 in the validation period (Figs. 10b and c). Similar to YTR, the triple-objective calibrations got

442 much smaller behavioral parameter sets (19 and 18 for measurement- and isoGSM-forced
443 calibration variants) than the dual-objective calibration (117) through 150 runs of the automatic
444 calibration program, indicating strongly increased identifiability of model parameters and
445 reduced uncertainty by the using of isotope data.

446 [Figure 9]

447 [Figure 10]

448 [Table 4]

449 3.3 Contributions of runoff components

450 Fig. 11 and Tables 5-6 compare the proportions of water sources in the annual water input
451 for runoff generation simulated by the behavioral parameter sets identified by the three
452 calibration variants. In the KR sub-basin (Fig. 11b and Table 6), rainfall provided the largest
453 volume of water source for runoff generation simulated by the three calibration variants
454 (44.2%-47.4%), followed by glacier meltwater (29.2%-33.8%). Snowmelt contributed the
455 lowest proportion of 22.0%-23.4% in the total water input. The two triple-objective calibrations
456 estimated very similar contributions of runoff component, and consistently estimated lower
457 proportions of glacier melt than the dual-objective calibration, which can be attributed to the
458 role of isotope data in regulating the contribution of strong-evaporated surface runoff
459 component fed by glacier melt to streamflow (Nan et al., 2021) by rejecting parameter sets that
460 estimated small proportions of rainfall but large proportions of glacier melt (as shown by the
461 error bar in Fig. 11b). Meanwhile, uncertainties of the estimated contributions were
462 significantly reduced (from 9.4% to 6.2% and 4.7%, Table 6) by integrating isotope data into
463 the model. Regarding the contributions of water sources to seasonal water input, snowmelt and
464 rainfall were the dominant water sources in spring and summer. Three water sources had similar
465 contributions during autumn. Glacier melt produced a relatively steady contribution of around
466 30%-35% throughout the year. Similar to the annual contributions, seasonal contributions of
467 snowmelt and rainfall estimated by the two triple-objective calibrations were larger than those
468 estimated by the dual-objective calibration, while the opposite holds true for the seasonal
469 contributions of glacier melt. The largest differences of the contributions estimated by the
470 different calibration variants go to the winter season (Table 6), which however had negligible
471 effect on the annual runoff regime because of the extremely low contribution of water input in
472 this season (<1%). Uncertainties of the runoff component contributions were reduced by
473 involving isotope calibration most significantly during summer, because the isotope data
474 brought more constraint on the rainfall-runoff processes, which played dominant role in summer.
475 The uncertainties of annual contributions were close to those of summer contributions because
476 of the large proportion of water input to annual runoff in summer (>60%). In contrast,
477 uncertainties of winter contributions estimated by the triple-objective calibration variants

478 tended to be larger than that estimated by the dual-objective calibration, due to the smaller
479 amount of total water input in winter as a result of lower contribution of meltwater estimated
480 by triple-objective variants.

481 In the YTR catchment, rainfall showed larger dominance on annual runoff than glacier and
482 snow meltwater with the mean contributions of 61.4%-69.6% (Fig. 11a and Table 5). The dual-
483 objective calibration and triple-objective calibration forced by measured isotope data estimated
484 similar annual contributions of rainfall (~62%), snowmelt (~11%) and glacier melt (~27%).
485 Nonetheless, the isoGSM-forced triple-objective calibration estimated significantly higher
486 mean proportion of rainfall (70%) but lower mean proportion of glacier melt (18%) by rejecting
487 the parameter sets that estimated rainfall contributions less than 60% and glacier melt
488 contributions more than 30%, which however were identified to be acceptable in the other two
489 calibration variants (as shown by the error bar in Fig. 11a). Difference of the glacier melt
490 contributions estimated by the two triple-objective calibration variants mainly resulted from the
491 difference of precipitation $\delta^{18}\text{O}$ inputs from the two datasets. The interpolated measurement
492 data tended to produce higher precipitation $\delta^{18}\text{O}$ in the middle and downstream regions of YTR
493 basin but lower values in the upstream region, compared to the corrected isoGSM data (Fig.
494 4b). Meanwhile, the precipitation input in the downstream region was higher than that occurred
495 in the upstream (Xu et al., 2017), thus resulting in higher average precipitation $\delta^{18}\text{O}$ over the
496 entire YTR of the interpolated measurement data. Consequently, larger contribution of glacier
497 melt with low isotope composition was estimated in the interpolated [measurementinterpolation-](#)
498 forced triple-objective calibration to counteract the effect of precipitation input with high
499 isotopic composition for matching the measured stream water $\delta^{18}\text{O}$. By involving isotope
500 simulation, both triple-objective variants significantly reduced the uncertainties of the
501 estimated contributions (from 11.9% to 8.6% and 8.9%, Table 5). Similar to the estimated
502 annual contributions, the isoGSM-forced triple-objective calibration estimated higher mean
503 proportion of rainfall, lower mean proportion of glacier melt and comparable mean proportion
504 of snowmelt in the four seasons, compared to the dual-objective calibration and triple-objective
505 calibration forced by measured isotope data. In general, rainfall was the dominant water input
506 source in summer and autumn, and snowmelt dominated the runoff in winter. The contributions
507 of rainfall and snowmelt to total water input were close in spring. Similar to KR catchment,
508 uncertainty of runoff component contribution was reduced by the isotope-involved calibrations
509 more significantly in seasons when rainfall played dominant roles.

510 [Figure 11]

511 [Table 5]

512 [Table 6]

513 4. Discussion

514 4.1 Uncertainties ~~of the simulations of water isotope signatures~~ and limitations of the 515 tracer-aided hydrological model

516 Integrating the simulations of water isotope signatures into the hydrological model
517 structure could help to make use of hydrological information additionally implied in the water
518 isotope data without introducing new model parameters for the runoff processes. However,
519 uncertainty of the simulation of water isotope in the tracer-aided hydrological model can be
520 caused by the following sources. First, the isotopic compositions of meltwater sources were
521 determined based on simplified assumptions, which however were hard to verify in a large
522 basin due to the limited field sampling work. The isotopic compositions of glacier melt were
523 assumed as constant throughout the modeling period due to the unavailability of glacier melting
524 water samples. Large number of studies reported that the isotope composition of glacier melt
525 had very small variability, and the value were much lower than that of precipitation (e.g., Boral
526 & Sen, 2020; Cable et al., 2011; He et al., 2019; Rai et al., 2019; Wang et al., 2016). Considering
527 that This could be reasonable because the changes of glacier elevation during the 10-year
528 modeling period were small, indicating that ice melt on the glacier surface in each of the
529 summer seasons occurred very likely from the same elevation bands with similar isotopic
530 compositions. the assumption on glacier melt isotope adopted in this study was reasonable.;
531 However, the assumed isotope composition of glacier melt will no doubt influence the
532 modelling result, especially the estimated contribution of water sources. Specifically, a lower
533 assumed value of glacier melt isotope composition led to a lower contribution of isotopic
534 depleted glacier melt runoff component. As for the snow meltwater, The isotopic evolution of
535 snow meltwater was simulated according to the mass balance of snowpack similarly with other
536 water storages. The isotope fractionation effect caused by the melt processes was inadequately
537 characterized in our model, which could lead to uncertainty in the simulation of snowmelt
538 isotope (Pu et al., 2020).

539 Second, the uncertainty of the precipitation isotope input data served as another uncertainty
540 source of the isotope simulation in the model. Although the isotope data itself had no influences
541 on the hydrological processes, the calibration procedure to fit the simulated stream isotope
542 signature with observation indeed affected the model simulations of runoff processes (Delavau
543 et al., 2017). For the sampling measurement-based forcing data, the uncertainty came from the
544 interpolation procedure. We used a linear interpolation method based on longitude and altitude
545 to estimate the precipitation isoscape. This could be reasonable in our study catchment because
546 these two factors characterize the major spatial pattern and altitude effect of precipitation
547 isotope in similar large-scale regions on TP (Liu et al., 2014). However, low availability of site
548 measurement data derived from the sparse water sampling network led to large uncertainty

549 of the interpolated result. [All the four sampling stations were located at around the same latitude,](#)
550 [and cannot reflect latitude effect on precipitation isotope \(Dansgaard, 1964\).](#) Measurements
551 from more water sampling sites are required in the future for the improvement of the
552 interpolation method. For the isoGSM data, uncertainty came from its coarse spatial resolution.
553 Although the isoGSM data bears the potential to capture spatial patterns of precipitation isotope
554 in large basins, the effect of regional topography on isotope was not reflected well in the current
555 product due to its rather coarse pixel size (~200km×200km). Consequently, developing
556 downscale methods that are applicable to mountainous catchments to extract regional isotope
557 estimates from iGCM products (such as iRCM in [Sturm et al., 2007](#)) might be helpful for the
558 tracer-aided hydrological modelling on the TP. Moreover, the bias-correction procedure based
559 on measurements from a sparse water sampling network inevitably brought uncertainty to the
560 corrected isoGSM data. The current sampling sites of precipitation are located along the river
561 channel with elevations lower than the contributing mountains, thus failing to involve isoGSM
562 estimates at high mountainous terrains into the correction procedure. [The terms used in Eq. 3](#)
563 [\(only elevation\) to correct isoGSM were different from that in Eq. 1 \(elevation and longitude\)](#)
564 [to interpolate the measurement data. The error of isoGSM tended to be larger in higher elevation](#)
565 [regions, because of the complex regional topography which cannot be captured well by the](#)
566 [coarse spatial resolution of isoGSM, but there was no mechanism making the error of isoGSM](#)
567 [change with longitude. Consequently, the term longitude was deprecated in Eq. 3 rather than](#)
568 [the interpolation equation. However, the choice of regression terms in interpolation and bias](#)
569 [correction undoubtedly had significant influence on the modelling result, which could be](#)
570 [another important source of uncertainty.](#)

571 [The modelling uncertainty is highly related to the model structure and parameters, and our](#)
572 [results indicated that the additional information from isotope data reduced uncertainty of](#)
573 [parameters. However, global climate changes are changing streamflow regimes on the TP \(e.g.,](#)
574 [Xu et al., 2019; Lin et al., 2020; Yong et al., 2021\), which may request a changing model](#)
575 [structure as well. In this study, the model structure was not modified, thus the changing](#)
576 [conditions were far less than adequately represented in the current model, due to lack of](#)
577 [adequate understanding of the influence of changing condition on runoff generation mechanism.](#)
578 [However, some of the changing underlying conditions can also be reflected by the parameters.](#)
579 [For example, frozen ground degradation can lead to a larger water storage capacity and higher](#)
580 [hydraulic conductivity, which can be reflected by the parameters WM, KKA and KKD in our](#)
581 [model. Meanwhile, the tracer-aided hydrological modelling method can also help diagnose the](#)
582 [model structure \(e.g., Birkel et al., 2011\), but such work has been only conducted in small](#)
583 [catchments due to the limited precipitation isotope input data in large scale. This study mainly](#)
584 [explored the utility of iGCM data on forcing tracer-aided model in large basins, thus provided](#)
585 [the potential to conduct the works improving model structure in large basin scale. For the](#)

586 [simulation in YTR basin in this study, the model was applied at a relatively short time scale](#)
587 [\(less than one decade\), during which the change condition was not an important issue. To](#)
588 [expand the result to a longer time scale and to predict the future streamflow trend, more work](#)
589 [is needed to consider the variation of model structures and parameters.](#)

590 **4.2 The value of spatial precipitation isotope data derived from iGCM for aiding** 591 **hydrological modeling in large basins**

592 Comparisons with the dual-objective calibration without isotope data indicated high value
593 of spatial precipitation isotope data for reducing modeling uncertainty. [To better understand the](#)
594 [role of isotope data, we analyzed the relationship between the behaviors of discharge and](#)
595 [isotope simulations obtained by the calibration without isotope \(dual-objective calibration\).](#)
596 [There was a trade-off between the two objectives \(Fig. 12a\). The highest \$NSE_{dis}\$ can reach](#)
597 [around 0.93, but the \$MAE_{iso}\$ was not good at the same time. When \$MAE_{iso}\$ reach relative best](#)
598 [values, the \$NSE_{dis}\$ was around 0.9, which ~~was exhibited still~~ a high-level performance as well.](#)
599 [The relationship between model performance and estimated glacier melt contribution was](#)
600 [further explored, and it was found that when the highest \$NSE_{dis}\$ was obtained, the contribution](#)
601 [of glacier melt was estimated as around 0.35~0.4, which was however estimated as around 0.2](#)
602 [when best \$MAE_{iso}\$ was obtained \(Fig. 12b and c\). The isotope composition of glacier melt was](#)
603 [assumed to be lower than the precipitation, thus an overestimated contribution of glacier melt](#)
604 [can lead to lower simulated river isotope than measurement. Consequently, calibration focusing](#)
605 [only on discharge may result in overestimated glacier melt, which can be rejected by the](#)
606 [behavior of isotope simulation. It is notable that the performance of isotope simulation is more](#)
607 [sensitive than discharge simulation to the runoff component and internal processes. When the](#)
608 [contribution of glacier melt is in a large range of 10-40%, the \$NSE_{dis}\$ can all be calibrated to a](#)
609 [high value \(\$>0.9\$ \) by adjusting other parameters, whereas the \$MAE_{iso}\$ gets worse significantly](#)
610 [when the proper contribution of water source is deviated.](#)

611 **[Figure 12]**

612 Model simulations forced by the two precipitation isotope datasets produced similar total
613 streamflow simulation in the YTR basin, but resulted in certain difference in the simulated
614 stream water isotopic composition and water source apportionments, which was consistent with
615 the findings in [Delavau et al. \(2017\)](#). The choice of precipitation isotope input data was
616 demonstrated to have large influence on the model performance. In this study, model
617 simulations forced by the corrected isoGSM data performed better than that driven by the
618 interpolated data of sampling measurement with respect to discharge and stream water isotope
619 simulations at internal hydrological stations. [The fact that model can simultaneously satisfy](#)
620 [multiple calibration objectives gave confidence in the model realization and robustness](#)
621 [\(McDonnell and Beven, 2014\), consequently resulting in the consistent model behavioral](#)

622 performances in both outlet and internal stations.

623 Beyond the model performance on discharge and isotope simulation, three aspects of
624 evidences indicated the results of model forced by isoGSM data to be more likely reasonable.
625 Firstly, Beyond that, the runoff component contributions estimated by the isoGSM-forced
626 triple-objective calibration were likely more reliable than those estimated by the dual-objective
627 and the measurementinterpolation-forced triple-objective calibrations. Contribution of glacier
628 melt to annual water input in the YTR basin was estimated as around 27% in the dual-objective
629 and the measurementinterpolation-forced triple-objective calibrations, which might not be
630 reasonable,was more unlike to be true considering the small glacier covered area ratio (2%).
631 Glacier melt contribution estimated by the isoGSM-forced triple-objective calibration was
632 lower than 20%, within the ranges reported bysimilarly to estimates in some previous studies
633 (Immerzeel et al., 2010; Bookhagen and Burbank, 2010; Zhang et al., 2013), and the finding
634 that glacier melt contributed a bit more than snowmelt was consistent with the result of Lutz et
635 al. (2014) during the similar period (1998-2007). Secondly, the average calibrated melting
636 threshold temperature (T_0) and glacier degree-day factor (DDF_G) of YTR basin obtained by the
637 isoGSM-forced triple-objective calibration were 0.75°C and $7.43\text{mm/d}^{\circ}\text{C}$. This was consistent
638 with the reported results estimated in a manner by glacier mass balance measurements, that the
639 YTR basin was in the region with DDF_G ranging from 6-9 $\text{mm/d}^{\circ}\text{C}$ estimated by the T_0 of 0°C
640 (Zhang et al., 2006). On the contrary, although the calibrated DDF_G obtained by dual-objective
641 and interpolation-forced triple-objective calibration were still within the range of 6-9 (7.98 and
642 $8.37 \text{ mm/ d}^{\circ}\text{C}$, respectively), the T_0 values were calibrated as -1.41 and -1.49°C , respectively,
643 much lower than the value adopted in Zhang et al. (2006), resulting in overestimated glacier
644 melt runoff. Thirdly, the THREW-t model also quantified the runoff component in terms of
645 runoff generation pathway, and divided the runoff into surface runoff and baseflow. The
646 contribution of baseflow was estimated as $29.26 \text{ km}^3/\text{yr}$ by the isoGSM-forced triple-objective
647 calibration, which was very close to the result ($30\text{km}^3/\text{yr}$) estimated by the groundwater model
648 MODFLOW-NWT independently from hydrological modeling approach reported in Yao et al.
649 (2021), whereas the baseflow estimated by dual-objective and interpolation-forced triple-
650 objective were much lower (24.04 and $22.47 \text{ km}^3/\text{yr}$, respectively). A more reliable baseflow
651 estimation likely helped improve the reasonability of modelling result, and reduce equifinality
652 by constraining the parameters related to groundwater.

653 This Above results indicated that the corrected isoGSM product served as a better choice
654 to force the tracer-aided hydrological model than the interpolated data of sampling
655 measurement. It is commonly difficult to estimate the precipitation isoscapes in large
656 mountainous catchments according to limited available site sampling data. Relatively, the
657 iGCM data has the advantage of presenting more spatial information of precipitation isotope
658 via physically simulating the processes of vapor transfer, condensation and supersaturation in

659 the atmosphere and their effects on precipitation isotope (Xi, 2014). Our results indicated that
660 even precipitation isotope measurements at only four sampling sites provided sounds good
661 ground data basis to correct the isoGSM isotope product in the study basin with a size of 2×10^5
662 km^2 . The condition was different in the KR sub-catchment, where the triple-objective variants
663 forced by two isotope datasets performed similarly with respect to discharge and isotope
664 simulation and runoff component contribution estimation. This is due to the much smaller
665 catchment area than the pixel size, thus the advantage of the spatial information provided by
666 isoGSM was not taken adequately. To develop a general strategy for establishing tracer-aided
667 in large basin, especially in the regions where ~~little~~ limited measured precipitation isotope data
668 is available, ~~little-as~~ less information from measurement data as possible was used to correct
669 the isoGSM data. Consequently, only the average value of measured isotope data was used to
670 correct the isoGSM (Eq. 2), and the seasonal characteristic of the bias was not considered
671 like (such as in Delavau et al., ~~-(2017)~~). Our results indicated that even being corrected by only
672 four average values, isoGSM can perform well on capturing seasonal fluctuation of
673 precipitation isotope and forcing tracer-aided model in YTR basin, thus bears the potential to
674 serve as input isotope data in data sparse regions. The influence of iGCM/iRCM product and
675 bias correction method was not discussed in detail ~~deeply~~ in this study, which is however an
676 important issue and need further exploration ~~in the future~~.

677 5. Conclusions

678 The utility of precipitation isotope input derived from the Isotopic General Circulation
679 Models (iGCM) product isoGSM in forcing the distributed tracer-aided hydrological model
680 THREW-t in a large basin of $2 \times 10^5 \text{km}^2$ on the Tibetan Plateau (TP) was investigated in this
681 ~~work~~ study. Model performance driven by the isoGSM data was evaluated by comparing with
682 simulations driven by precipitation isotope measurements from a sparse sampling network. Our
683 main findings are:

684 (1) Spatial precipitation isotope data derived from the Isotopic General Circulation Models
685 helped to reduce modeling uncertainty and improve parameter identifiability, in comparison to
686 a calibration method using discharge and snow cover area fraction without any information of
687 water isotope. The developed tracer-aided hydrological model forced by the isoGSM data
688 showed high values for robustly representing runoff processes in large mountainous catchments.

689 (2) Model parameters estimated by the isoGSM data corrected using site sampling
690 measurements of precipitation isotope presented higher transferability to nested sub-basins and
691 produced higher model performance in the validation period than that estimated by the
692 interpolated isotope data from site sampling measurement. The smaller uncertainty ranges of
693 model simulations in nested sub-basins forced by the corrected isoGSM data further indicated
694 that the corrected isoGSM data served as a better choice to provide informative spatial

695 precipitation isotope in large basins than the interpolated data from site sampling measurements.
696 (3) Using the corrected isoGSM data improved the quantification of contributions of runoff
697 components to streamflow on both annual and seasonal scales. Model calibration procedure
698 forced by the corrected isoGSM data successfully rejected parameter sets that estimated
699 overestimation of glacier melt contribution, indicating that precipitation isotope measurements
700 at only four sampling sites along the river channel provided a good ground data basis to correct
701 the isoGSM product in the study catchment.

702 **Code/Data availability**

703 The isotope data and the code of THREW-t model used in this study are available by contacting
704 the authors.

705 **Author contribution**

706 YN, ZH and FT conceived the idea; ZW provided the isoGSM data; LT provided the
707 measurement isotope data; YN, ZH and FT conducted analysis; ZW and LT provided comments
708 on the analysis; all the authors contributed to writing and revisions.

709 **Competing interests**

710 The authors declare that they have no conflict of interest.

711 **Acknowledgements**

712 This study was supported by the National Key R&D Program of China (2018YFC1508103)
713 and the National Science Foundation of China (92047301). The authors thank all the
714 organizations and scientists for the contribution of data used in this work. All the data used in
715 this study will be available on request from the corresponding author (tianfq@tsinghua.edu.cn).

716 **Financial support**

717 This study was supported by the National Key R&D Program of China (2018YFC1508103)
718 and the National Science Foundation of China (92047301).

719

720 **References**

- 721 Ala-aho, P., Tetzlaff, D., McNamara, J. P., Laudon, H., & Soulsby, C. (2017). Using isotopes to
722 constrain water flux and age estimates in snow-influenced catchments using the STARR
723 (Spatially distributed Tracer-Aided Rainfall–Runoff) model. *Hydrology and Earth System
724 Sciences*, 21(10), 5089-5110. doi:10.5194/hess-21-5089-2017
- 725 Birkel, C., & Soulsby, C. (2015). Advancing tracer-aided rainfall-runoff modelling: a review of
726 progress, problems and unrealised potential. *Hydrological Processes*, 29(25), 5227-5240.
727 doi:10.1002/hyp.10594
- 728 Birkel, C., Tetzlaff, D., Dunn, S. M., & Soulsby, C. (2011). Using time domain and geographic
729 source tracers to conceptualize streamflow generation processes in lumped rainfall-runoff
730 models. *Water Resources Research*, 47(2). doi:10.1029/2010wr009547
- 731 Bookhagen, B., & Burbank, D. W. (2010). Toward a complete Himalayan hydrological budget:
732 Spatiotemporal distribution of snowmelt and rainfall and their impact on river discharge.
733 *Journal of Geophysical Research*, 115(F3). doi:10.1029/2009jf001426
- 734 [Boral, S., & Sen, I. S. \(2020\). Tracing ‘Third Pole’ ice meltwater contribution to the Himalayan
735 rivers using oxygen and hydrogen isotopes. *Geochem. Perspect. Lett.*, 13, 48-53.](#)
- 736 Cable, J., Ogle, K., & Williams, D. (2011). Contribution of glacier meltwater to streamflow in
737 the Wind River Range, Wyoming, inferred via a Bayesian mixing model applied to isotopic
738 measurements. *Hydrological Processes*, 25(14), 2228-2236.
- 739 Capell, R., Tetzlaff, D., & Soulsby, C. (2012). Can time domain and source area tracers reduce
740 uncertainty in rainfall-runoff models in larger heterogeneous catchments? *Water
741 Resources Research*, 48(9). doi:10.1029/2011wr011543
- 742 Chen, X., Long, D., Liang, S., He, L., Zeng, C., Hao, X., & Hong, Y. (2018). Developing a
743 composite daily snow cover extent record over the Tibetan Plateau from 1981 to 2016
744 using multisource data. *Remote Sensing of Environment*, 215, 284-299.
745 doi:10.1016/j.rse.2018.06.021
- 746 [Dansgaard, W.: Stable isotopes in precipitation, *Tellus*, 16, 436–468, 1964.](#)
- 747 Delavau, C. J., Stadnyk, T., & Holmes, T. (2017). Examining the impacts of precipitation
748 isotope input ($\delta^{18}\text{O}$) on distributed, tracer-aided hydrological modelling. *Hydrology and
749 Earth System Sciences*, 21(5), 2595-2614. doi:10.5194/hess-21-2595-2017

750 Didan, K. (2015). MOD13A3 MODIS/Terra vegetation Indices Monthly L3 Global 1km SIN
751 Grid V006 [Data set]. NASA EOSDIS Land Processes DAAC. Accessed 2020-01-01 from
752 <https://doi.org/10.5067/MODIS/MOD13A3.006>

753 Dong, W., Lin, Y., Wright, J. S., Ming, Y., Xie, Y., Wang, B., . . . Xu, F. (2016). Summer rainfall
754 over the southwestern Tibetan Plateau controlled by deep convection over the Indian
755 subcontinent. *Nature Communications*, 7. doi:10.1038/ncomms10925

756 Duethmann, D., Bolch, T., Farinotti, D., Kriegel, D., Vorogushyn, S., Merz, B., . . . Güntner, A.
757 (2015). Attribution of streamflow trends in snow and glacier melt-dominated catchments
758 of the Tarim River, Central Asia. *Water Resources Research*, 51(6), 4727-4750.
759 doi:10.1002/2014wr016716

760 Eriksson, D., Bindel, D., & Shoemaker, C. (2015). Surrogate optimization toolbox (pysot).

761 Gao, J., Tian, L. D., & Liu, Y. Q. (2009). Oxygen isotope variation in the water cycle of the
762 Yamdrok-tso Lake Basin in southern betan Plateau. *Chinese Science Bulletin*, 54(15),
763 2153-2159.

764 Gupta, H. V., Wagener, T., & Liu, Y. (2008). Reconciling theory with observations: elements of
765 a diagnostic approach to model evaluation. *Hydrological Processes*, 22(18), 3802-3813.
766 doi:10.1002/hyp.6989

767 He, Z., Unger-Shayesteh, K., Vorogushyn, S., Weise, S. M., Kalashnikova, O., Gafurov, A., . . .
768 Merz, B. (2019). Constraining hydrological model parameters using water isotopic
769 compositions in a glacierized basin, Central Asia. *Journal of Hydrology*, 571, 332-348.
770 doi:10.1016/j.jhydrol.2019.01.048

771 He, Z., Vorogushyn, S., Unger-Shayesteh, K., Gafurov, A., Kalashnikova, O., Omorova, E., &
772 Merz, B. (2018). The Value of Hydrograph Partitioning Curves for Calibrating
773 Hydrological Models in Glacierized Basins. *Water Resources Research*, 54(3), 2336-2361.
774 doi:10.1002/2017wr021966

775 He, Z. H., Tian, F. Q., Gupta, H. V., Hu, H. C., & Hu, H. P. (2015). Diagnostic calibration of a
776 hydrological model in a mountain area by hydrograph partitioning. *Hydrology and Earth
777 System Sciences*, 19(4), 1807-1826. doi:10.5194/hess-19-1807-2015

778 He, Z., Yang, L., Tian, F., Ni, G., Hou, A., & Lu, H. (2017). Intercomparisons of Rainfall
779 Estimates from TRMM and GPM Multisatellite Products over the Upper Mekong River
780 Basin. *Journal of Hydrometeorology*, 18(2), 413-430. doi:10.1175/jhm-d-16-0198.1

- 781 Hindshaw, R. S., Tipper, E. T., Reynolds, B. C., Lemarchand, E., Wiederhold, J. G., Magnusson,
782 J., . . . Bourdon, B. (2011). Hydrological control of stream water chemistry in a glacial
783 catchment (Damma Glacier, Switzerland). *Chemical Geology*, 285(1-4), 215-230.
784 doi:10.1016/j.chemgeo.2011.04.012
- 785 Immerzeel, W. W., Pellicciotti, F., & Bierkens, M. F. P. (2013). Rising river flows throughout
786 the twenty-first century in two Himalayan glacierized watersheds. *Nature Geoscience*, 6(9),
787 742-745. doi:10.1038/ngeo1896
- 788 Immerzeel, W. W., van Beek, L. P. H., & Bierkens, M. F. P. (2010). Climate Change Will Affect
789 the Asian Water Towers. *Science*, 328(5984), 1382-1385. doi:10.1126/science.1183188
- 790 Kanamitsu, M., Kumar, A., Juang, H. M. H., Schemm, J. K., Wang, W. Q., Yang, F. L., . . . Ji,
791 M. (2002). NCEP dynamical seasonal forecast system 2000. *Bulletin of the American*
792 *Meteorological Society*, 83(7), 1019-+. doi:10.1175/1520-
793 0477(2002)083<1019:Ndsfs>2.3.Co;2
- 794 Li Z., Qi, F., Zongjie, L., Ruifeng, Y., Juan, G., & Yuemin, L. (2019). Climate background, fact
795 and hydrological effect of multiphase water transformation in cold regions of the Western
796 China: A review. *Earth-Science Reviews*, 190, 33-57. doi:10.1016/j.earscirev.2018.12.004
- 797 Lin, L., Gao, M., Liu, J., Wang, J., Wang, S., Chen, X., & Liu, H. (2020). Understanding the
798 effects of climate warming on streamflow and active groundwater storage in an alpine
799 catchment: the upper Lhasa River. *Hydrology and Earth System Sciences*, 24(3), 1145-
800 1157.
- 801 Liu, J., Song, X., Yuan, G., Sun, X., & Yang, L. (2014). Stable isotopic compositions of
802 precipitation in China. *Tellus Series B-Chemical and Physical Meteorology*, 66.
803 doi:10.3402/tellusb.v66.22567
- 804 Liu S. (2012). The second glacier inventory dataset of China (version 1.0) (2006-2011) [Data
805 set]. National Tibetan Plateau Data Center. Accessed 2020-01-01 from
806 <https://doi.org/10.3972/glacier.001.2013.db>.
- 807 Liu, Z., Tian, L., Yao, T., Gong, T., Yin, C., & Yu, W. (2007). Temporal and spatial variations
808 of delta O-18 in precipitation of the Yarlung Zangbo River Basin. *Journal of Geographical*
809 *Sciences*, 17(3), 317-326. doi:10.1007/s11442-007-0317-1
- 810 Lutz, A. F., Immerzeel, W. W., Shrestha, A. B., & Bierkens, M. F. P. (2014). Consistent increase
811 in High Asia's runoff due to increasing glacier melt and precipitation. *Nature Climate*

812 Change, 4(7), 587-592. doi:10.1038/nclimate2237

813 Masood, M., Yeh, P. J. F., Hanasaki, N., & Takeuchi, K. (2015). Model study of the impacts of
814 future climate change on the hydrology of Ganges–Brahmaputra–Meghna basin.
815 Hydrology and Earth System Sciences, 19(2), 747-770. doi:10.5194/hess-19-747-2015

816 McDonnell, J. J. , & Beven, K. . (2014). Debates—the future of hydrological sciences: a
817 (common) path forward? a call to action aimed at understanding velocities, celerities and
818 residence time distributions of the headwater hydrograph. Water Resources Research,
819 50(6).

820 McGuire, K. J., Weiler, M., & McDonnell, J. J. (2007). Integrating tracer experiments with
821 modeling to assess runoff processes and water transit times. Advances in Water Resources,
822 30(4), 824-837.

823 Myneni, R., Knyazikhin, Y., Park, T. (2015). MOD15A2H MODIS/Terra Leaf Area
824 Index/FPAR 8-Day L4 Global 500m SIN Grid V006 [Data set]. NASA EOSDIS Land
825 Processes DAAC. Accessed 2020-01-01 from
826 <https://doi.org/10.5067/MODIS/MOD15A2H.006>

827 Nan, Y., Tian, L., He, Z., Tian, F., & Shao, L. (2021). The value of water isotope data on
828 improving process understanding in a glacierized catchment on the Tibetan Plateau.
829 Hydrology and Earth System Sciences, 25(6), 3653-3673.

830 Noone, D., & Sturm, C. (2010). Comprehensive Dynamical Models of Global and Regional
831 Water Isotope Distributions.

832 Pu, T., Wang, K., Kong, Y., Shi, X., Kang, S., Huang, Y., . . . Cuntz, M. (2020). Observing and
833 Modeling the Isotopic Evolution of Snow Meltwater on the Southeastern Tibetan Plateau.
834 Water Resources Research, 56(9). doi:10.1029/2019wr026423

835 Rai, S. P., Singh, D., Jacob, N., Rawat, Y. S., & Arora, M. (2019). Identifying contribution of
836 snowmelt and glacier melt to the Bhagirathi River (Upper Ganga) near snout of the
837 Gangotri Glacier using environmental isotopes. Catena, 173, 339-351.

838 Reggiani, P., Hassanizadeh, S. M., Sivapalan, M., & Gray, W. G. (1999). A unifying framework
839 for watershed thermodynamics: constitutive relationships. Advances in Water Resources,
840 23(1), 15-39.

841 Schaner, N., Voisin, N., Nijssen, B., & Lettenmaier, D. P. (2012). The contribution of glacier

842 melt to streamflow. *Environmental Research Letters*, 7(3). doi:10.1088/1748-
843 9326/7/3/034029

844 Son, K., & Sivapalan, M. (2007). Improving model structure and reducing parameter
845 uncertainty in conceptual water balance models through the use of auxiliary data. *Water*
846 *Resources Research*, 43(1). doi:10.1029/2006wr005032

847 Stadnyk, T. A., Delavau, C., Kouwen, N., & Edwards, T. W. D. (2013). Towards hydrological
848 model calibration and validation: simulation of stable water isotopes using the
849 isoWATFLOOD model. *Hydrological Processes*, 27(25), 3791-3810.
850 doi:10.1002/hyp.9695

851 Sturm, C., Hoffmann, G., & Langmann, B. (2007). Simulation of the stable water isotopes in
852 precipitation over South America: Comparing regional to global circulation models.
853 *Journal of Climate*, 20(15), 3730-3750. doi:10.1175/jcli4194.1

854 Sturm, K., Hoffmann, G., Langmann, B., & Stichler, W. (2005). Simulation of delta O-18 in
855 precipitation by the regional circulation model REMOiso. *Hydrological Processes*, 19(17),
856 3425-3444. doi:10.1002/hyp.5979

857 Su, F., Zhang, L., Ou, T., Chen, D., Yao, T., Tong, K., & Qi, Y. (2016). Hydrological response
858 to future climate changes for the major upstream river basins in the Tibetan Plateau. *Global*
859 *and Planetary Change*, 136, 82-95. doi:10.1016/j.gloplacha.2015.10.012

860 Tian, F., Hu, H., Lei, Z., & Sivapalan, M. (2006). Extension of the Representative Elementary
861 Watershed approach for cold regions via explicit treatment of energy related processes.
862 *Hydrology and Earth System Sciences*, 10(5), 619-644. doi:10.5194/hess-10-619-2006

863 Tian, F., Hu, H., & Lei, Z. (2008). Thermodynamic watershed hydrological model: Constitutive
864 relationship. *Science in China Series E: Technological Sciences*, 51(9), 1353-1369.

865 Tian, F., Xu, R., Nan, Y., Li, K., & He, Z. (2020). Quantification of runoff components in the
866 Yarlung Tsangpo River using a distributed hydrological model. *Advances in Water*
867 *Science*, 31(3), 324-336.

868 Wang, C., Dong, Z., Qin, X., Zhang, J., Du, W., & Wu, J. (2016). Glacier meltwater runoff
869 process analysis using δD and $\delta^{18}O$ isotope and chemistry at the remote Laohugou
870 glacier basin in western Qilian Mountains, China. *Journal of Geographical Sciences*, 26(6),
871 722-734.

- 872 Wang, X., Zhang, X., Zhang, W., Zhang, X., & Luo, Z. (2017). Comparison on Spatial
873 Distribution of Hydrogen and Oxygen Stable Isotope GCM Simulation in Global
874 Precipitation. *Advance in Earth Sciences*, 32(9), 983-995.
- 875 Wolfe, B. B., Karst-Riddoch, T. L., Hall, R. I., Edwards, T. W. D., English, M. C., Palmini,
876 R., . . . Vardy, S. R. (2007). Classification of hydrological regimes of northern floodplain
877 basins (Peace -Athabasca Delta, Canada) from analysis of stable isotopes (δ O-18,
878 δ H-2) and water chemistry. *Hydrological Processes*, 21(2), 151-168.
879 doi:10.1002/hyp.6229
- 880 Xi, X. (2014). A Review of Water Isotopes in Atmospheric General Circulation Models: Recent
881 Advances and Future Prospects. *International Journal of Atmospheric Sciences*, 2014, 1-
882 16. doi:10.1155/2014/250920
- 883 Xu, M., Kang, S., Wang, X., Pepin, N., & Wu, H. (2019). Understanding changes in the water
884 budget driven by climate change in cryospheric-dominated watershed of the northeast
885 Tibetan Plateau, China. *Hydrological processes*, 33(7), 1040-1058.
- 886 Xu, R., Hu, H., Tian, F., Li, C., & Khan, M. Y. A. (2019). Projected climate change impacts on
887 future streamflow of the Yarlung Tsangpo-Brahmaputra River. *Global and Planetary
888 Change*, 175, 144-159. doi:10.1016/j.gloplacha.2019.01.012
- 889 Xu, R., Tian, F., Yang, L., Hu, H., Lu, H., & Hou, A. (2017). Ground validation of GPM IMERG
890 and TRMM 3B42V7 rainfall products over southern Tibetan Plateau based on a high-
891 density rain gauge network. *Journal of Geophysical Research: Atmospheres*, 122(2), 910-
892 924. doi:10.1002/2016jd025418
- 893 Yang, K., He, J., Tang, W., Qin, J., & Cheng, C. C. K. (2010). On downward shortwave and
894 longwave radiations over high altitude regions: Observation and modeling in the Tibetan
895 Plateau. *Agricultural and Forest Meteorology*, 150(1), 38-46.
896 doi:10.1016/j.agrformet.2009.08.004
- 897 Yao, T., Masson-Delmotte, V., Gao, J., Yu, W., Yang, X., Risi, C., . . . Hou, S. (2013). A review
898 of climatic controls on δ 18O in precipitation over the Tibetan Plateau: Observations and
899 simulations. *Reviews of Geophysics*, 51(4), 525-548. doi:10.1002/rog.20023
- 900 Yao, Y., Zheng, C., Andrews, C. B., Scanlon, B. R., Kuang, X., Zeng, Z., ... & Li, G. (2021).
901 Role of Groundwater in Sustaining Northern Himalayan Rivers. *Geophysical Research
902 Letters*, 48(10), e2020GL092354.

- 903 Yong, B., Wang, C. Y., Chen, J., Chen, J., Barry, D. A., Wang, T., & Li, L. (2021). Missing water
904 from the Qiangtang Basin on the Tibetan Plateau. *Geology*.
- 905 Yoshimura, K., Kanamitsu, M., Noone, D., & Oki, T. (2008). Historical isotope simulation
906 using Reanalysis atmospheric data. *Journal of Geophysical Research*, 113(D19).
907 doi:10.1029/2008jd010074
- 908 Zhang, F., Liu, J., Gong, T., & Wang, H. (2006a). Hydrological Regime of the Karuxung
909 Watershed in North Himalayas. *Acta Geographica Sinica*, 61(11), 1141-1148.
- 910 Zhang, F., Zhang, H., Hagen, S. C., Ye, M., Wang, D., Gui, D., . . . Liu, J. (2015). Snow cover
911 and runoff modelling in a high mountain catchment with scarce data: effects of
912 temperature and precipitation parameters. *Hydrological Processes*, 29(1), 52-65.
913 doi:10.1002/hyp.10125
- 914 Zhang, L., Su, F., Yang, D., Hao, Z., & Tong, K. (2013). Discharge regime and simulation for
915 the upstream of major rivers over Tibetan Plateau. *Journal of Geophysical Research:
916 Atmospheres*, 118(15), 8500-8518. doi:10.1002/jgrd.50665
- 917 Zhang, Y., Liu, S., & Ding, Y. (2006b). Spatial variation of degree-day factors on the observed
918 glaciers in western China. *ACTA GEOGRAPHICA SINICA-CHINESE EDITION*-, 61(1),
919 89.
- 920 Zhao, L., Xiao, H., Zhou, M., Cheng, G., Wang, L., Yin, L., & Ren, J. (2012). Factors
921 controlling spatial and seasonal distributions of precipitation d18O in China. *Hydrological
922 Processes*, 26(1), 143-152. doi:10.1002/hyp.8118
- 923

924 **List of figures**

925 **Figure 1.** Location and topography of (a) Tibetan Plateau, (b) Yarlung Tsangpo River basin and
926 (c) Karuxung catchment.

927 **Figure 2.** The scatter diagrams between original/corrected isoGSM and measured isotope data
928 in YTR basin (subfigures a and b) and KR catchment (subfigures c and d)

929 **Figure 3.** Temporal variations of precipitation $\delta^{18}\text{O}$ derived from measured and isoGSM data
930 in YTR basin (subfigure a) and KR catchment (subfigure b)

931 **Figure 4.** Comparisons of the amount weighted averages of precipitation $\delta^{18}\text{O}$ on 63 REWs in
932 the YTR basin by longitude (a) and elevation (b).

933 [Figure 5. Spatial distribution of average precipitation isotope composition obtained by \(a\)](#)
934 [interpolated measurement data and \(b\) corrected isoGSM.](#)

935 **Figure 6.** Uncertainty ranges of discharge ([Nuxia station](#)) and SCA simulations in YTR basin
936 during calibration and validation periods produced by the behavioral parameter sets of the dual-
937 objective (subfigure a and b), [measurementinterpolation](#)-forced triple-objective (subfigure c
938 and d), and isoGSM-forced triple-objective (subfigure e and f) calibration variants. The
939 discharge data is hidden for the data security policy.

940 **Figure 7.** Uncertainty ranges of stream water $\delta^{18}\text{O}$ simulations at four stations in 2005 produced
941 by the behavioral parameter sets of the dual-objective (a), [measurementinterpolation](#)-forced
942 triple-objective (b), and isoGSM-forced triple-objective (c) calibration variants.

943 **Figure 8.** Uncertainty ranges of discharge simulations at Yangcun and Nugesha stations
944 produced by the behavioral parameter sets of the dual-objective (subfigure a and b),
945 [measurementinterpolation](#)-forced triple-objective (subfigure c and d), and isoGSM-forced
946 triple-objective (subfigure e and f) calibration variants.

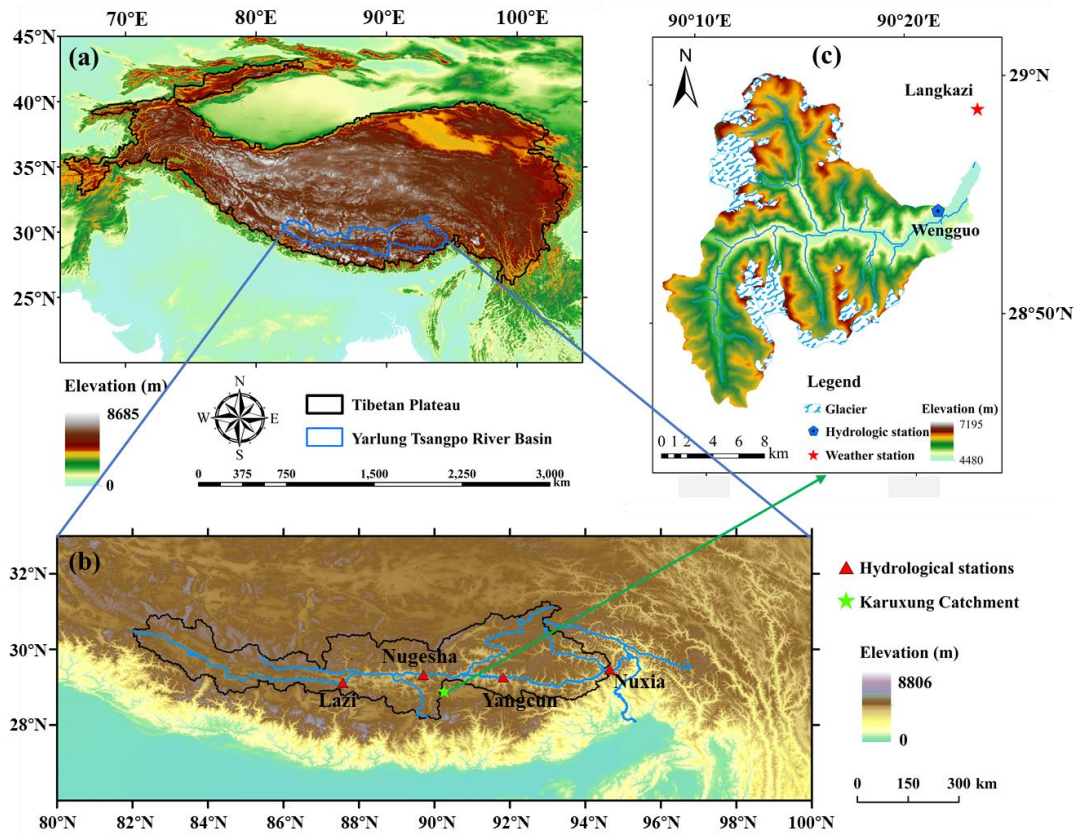
947 **Figure 9.** Uncertainty ranges of discharge and SCA simulations in KR catchment during
948 calibration and validation periods produced by the behavioral parameter sets of the dual-
949 objective (subfigure a and b), [measurementinterpolation](#)-forced triple-objective (subfigure c
950 and d), and isoGSM-forced triple-objective (subfigure e and f) calibration variants.

951 **Figure 10.** Uncertainty ranges of stream water $\delta^{18}\text{O}$ simulations in KR catchment during
952 calibration and validation periods produced by the behavioral parameter sets of the dual-
953 objective (a), [measurementinterpolation](#)-forced triple-objective (b), and isoGSM-forced triple-
954 objective (c) calibration variants.

955 **Figure 11.** Average proportion and corresponding uncertainty ranges of different water sources
956 in the annual water input for runoff generation estimated by different calibration variants in (a)
957 YTR and (b) KR catchments.

958 [Figure 12. The relationships between \(a\) MAE_{iso} and NSE_{dis}, \(b\) NSE_{dis} and glacier melt](#)
959 [contribution and \(c\) MAE_{iso} and glacier melt contribution.](#)

960



962

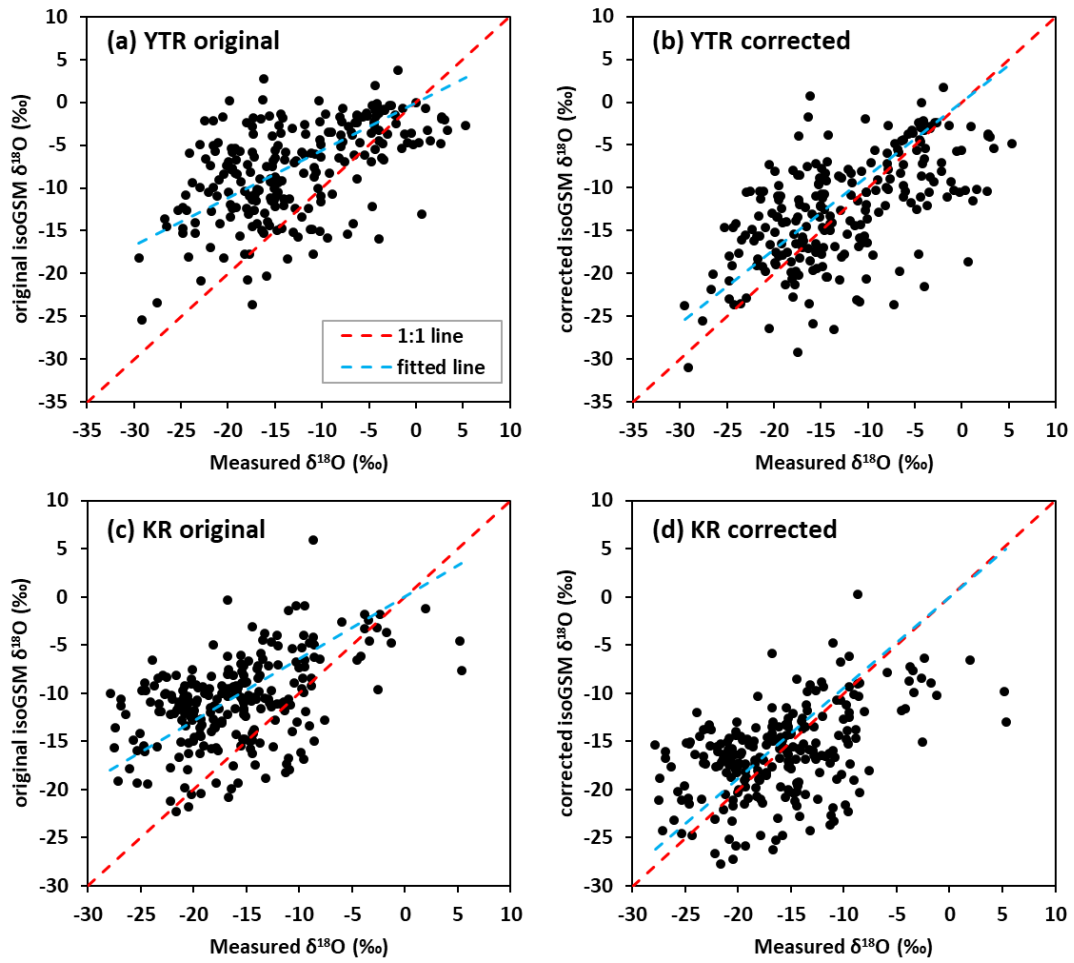
963

Figure 1. Location and topography of (a) Tibetan Plateau, (b) Yarlung Tsangpo River basin and

964

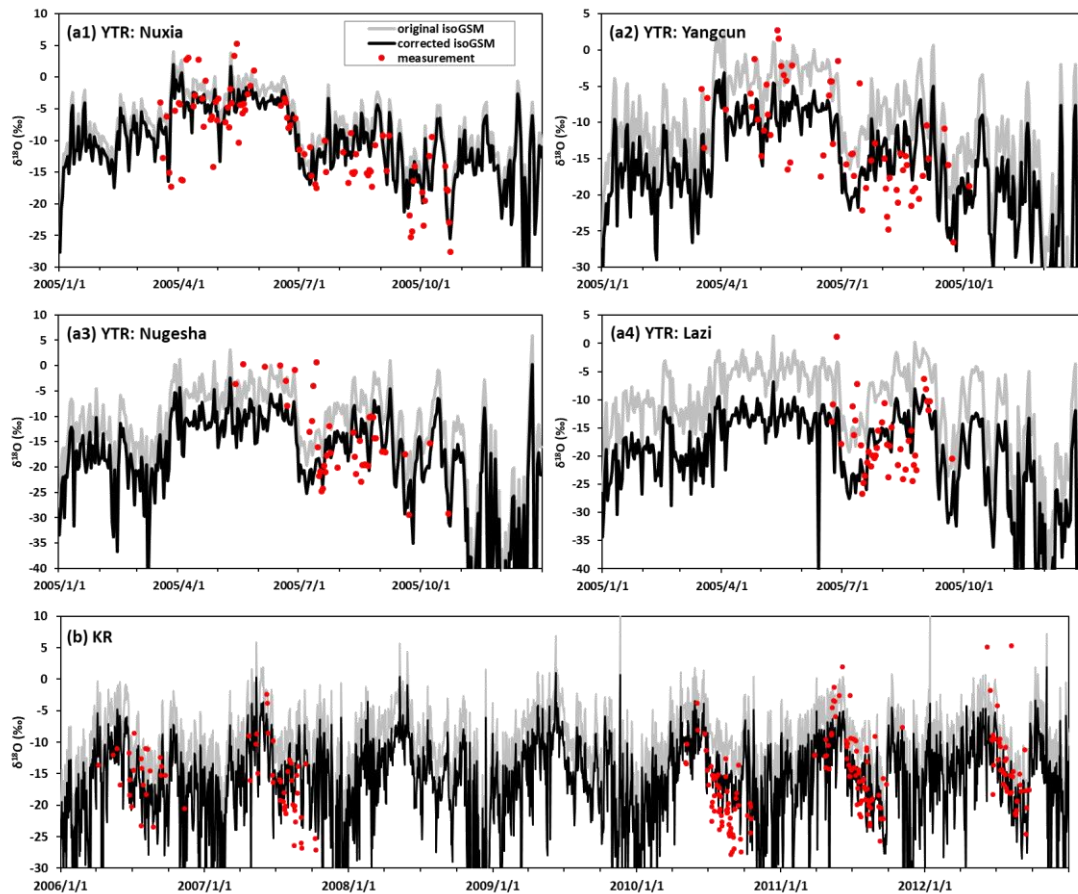
(c) Karuxung catchment

965



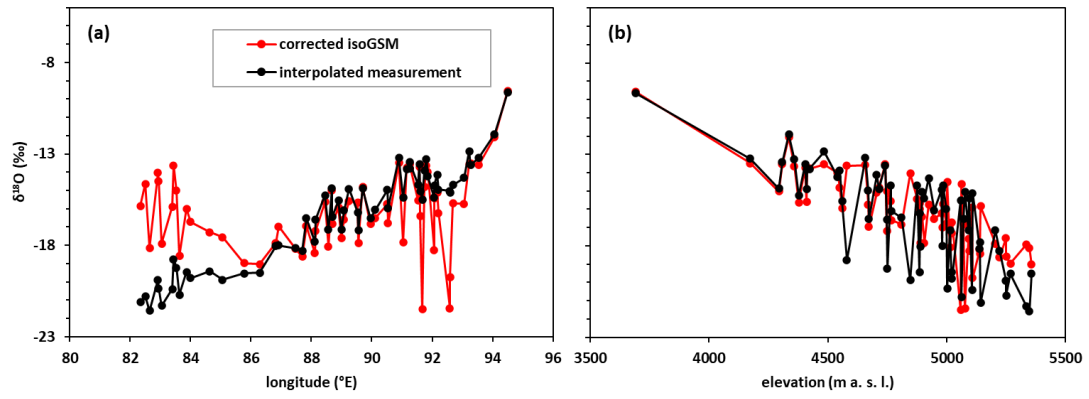
966
 967
 968
 969

Figure 2. The scatter diagrams between original/corrected isoGSM and measured isotope data in YTR basin (subfigures a and b) and KR catchment (subfigures c and d).



970

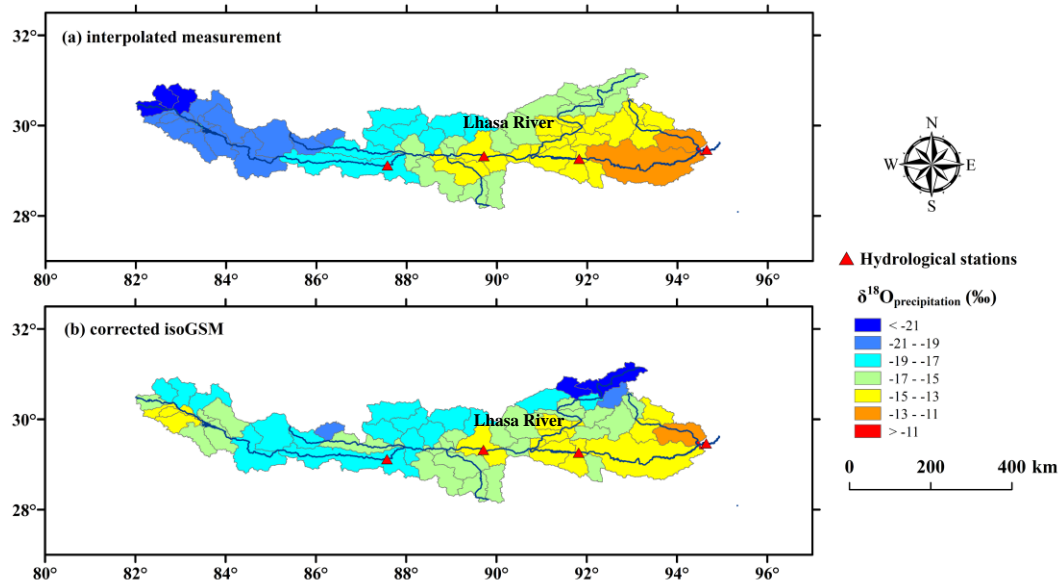
971 **Figure 3.** Temporal variations of precipitation $\delta^{18}\text{O}$ derived from measured and isoGSM data
 972 in YTR basin (subfigure a) and KR catchment (subfigure b).
 973



974

975 **Figure 4.** Comparisons of the amount weighted averages of precipitation $\delta^{18}\text{O}$ on 63 REWs in
 976 the YTR basin by longitude (a) and elevation (b).

977



978

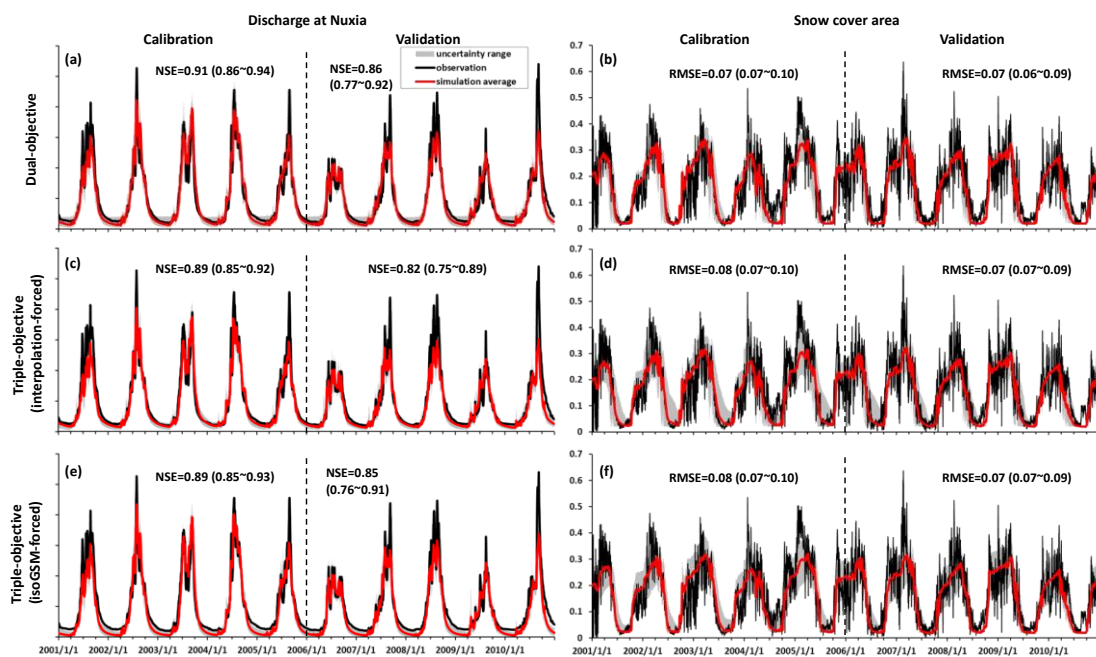
979 [Figure 5. Spatial distribution of average precipitation isotope composition obtained by \(a\)](#)

980 [interpolated measurement data and \(b\) corrected isoGSM.](#)

981

982

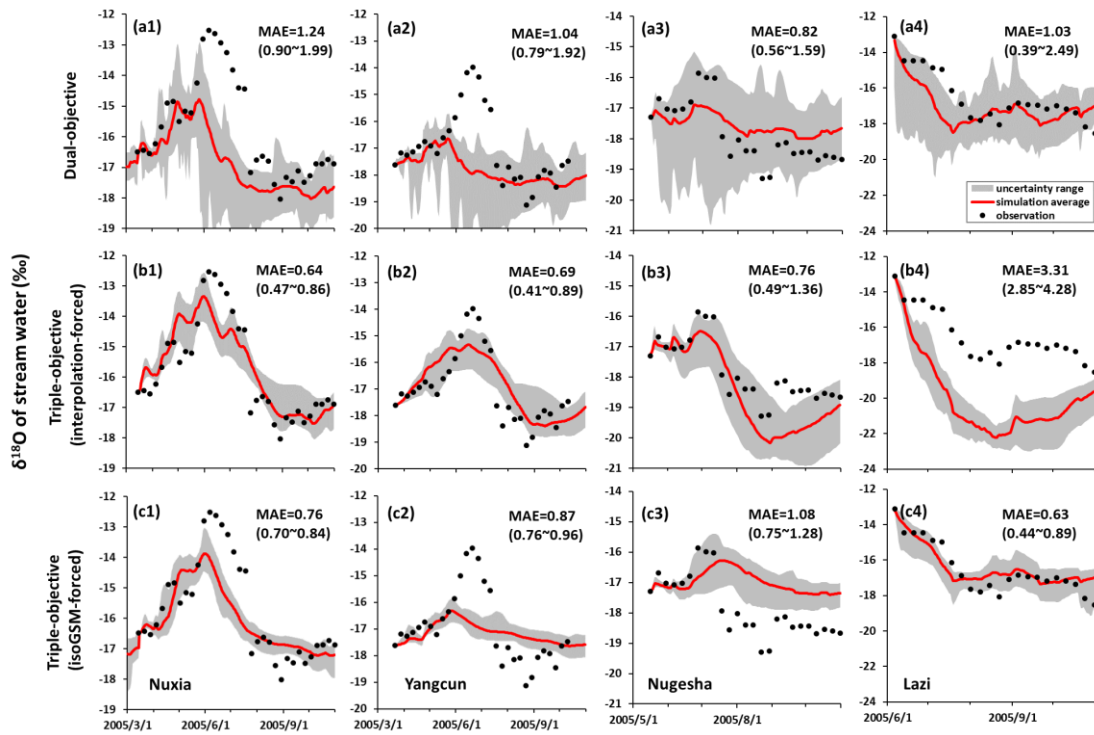
983



984

985 **Figure 6.** Uncertainty ranges of discharge ([Nuxia station](#)) and SCA simulations in YTR basin
986 during calibration and validation periods produced by the behavioral parameter sets of the dual-
987 objective (subfigure a and b), [measurement interpolation](#)-forced triple-objective (subfigure c
988 and d), and isoGSM-forced triple-objective (subfigure e and f) calibration variants. The scale
989 of discharge axis is hidden due to data security policy.

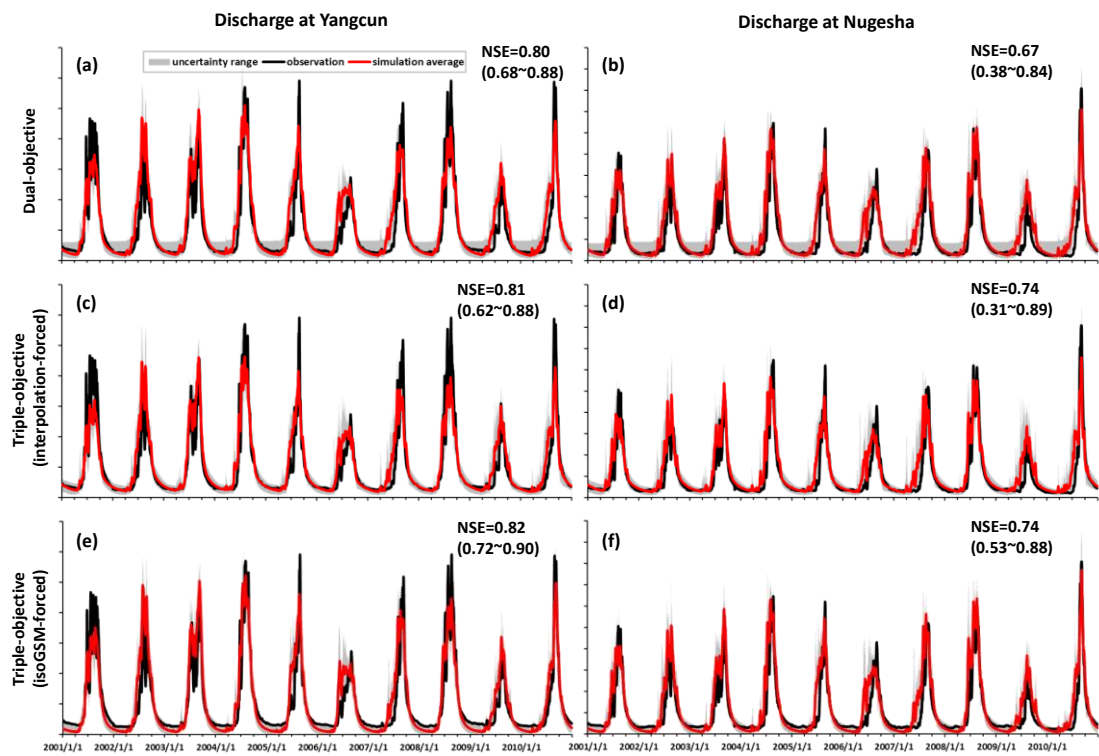
990



992

993 **Figure 7.** Uncertainty ranges of stream water $\delta^{18}\text{O}$ simulations at four stations in 2005 produced
 994 by the behavioral parameter sets of the dual-objective (a), [measurementinterpolation](#)-forced
 995 triple-objective (b), and isoGSM-forced triple-objective (c) calibration variants.

996



998

999

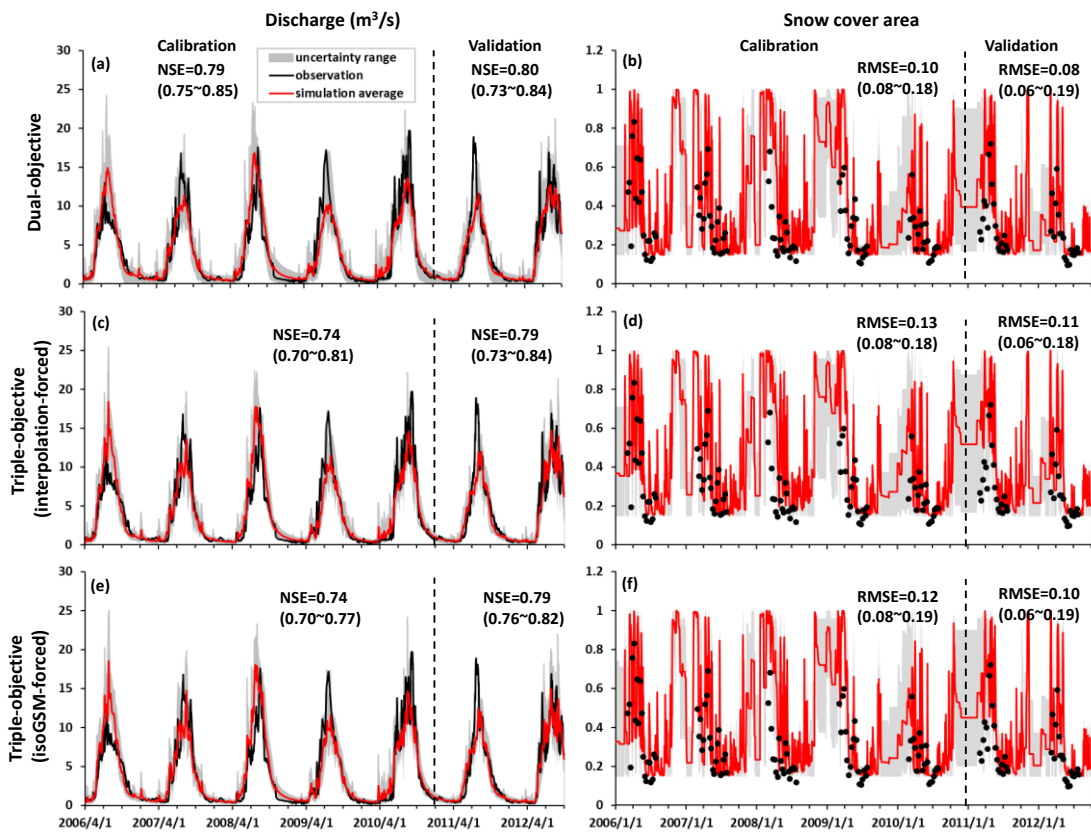
1000

1001

1002

1003

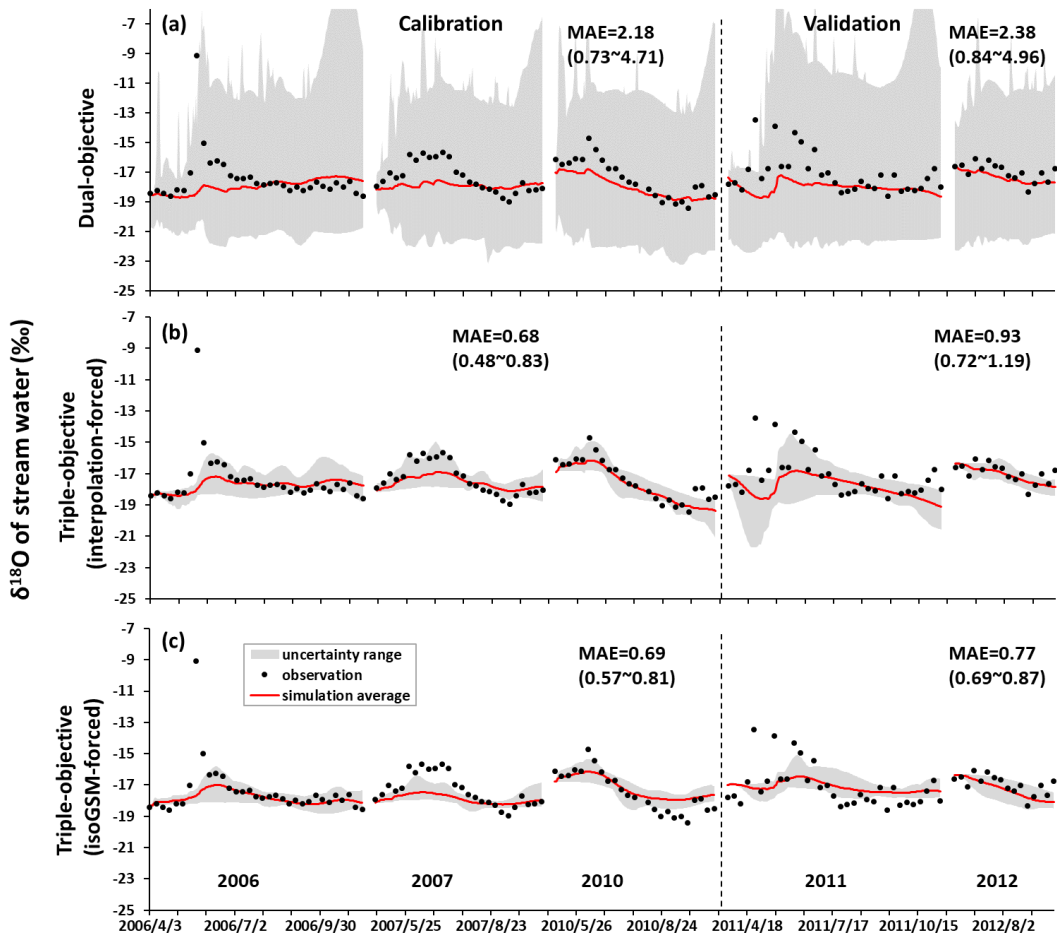
Figure 8. Uncertainty ranges of discharge simulations at Yangcun and Nugesha stations produced by the behavioral parameter sets of the dual-objective (subfigure a and b), [measurement interpolation](#)-forced triple-objective (subfigure c and d), and isoGSM-forced triple-objective (subfigure e and f) calibration variants.



1005

1006 **Figure 9.** Uncertainty ranges of discharge and SCA simulations in KR catchment during
 1007 calibration and validation periods produced by the behavioral parameter sets of the dual-
 1008 objective (subfigure a and b), [measurement interpolation](#)-forced triple-objective (subfigure c
 1009 and d), and isoGSM-forced triple-objective (subfigure e and f) calibration variants.

1010



1012

1013

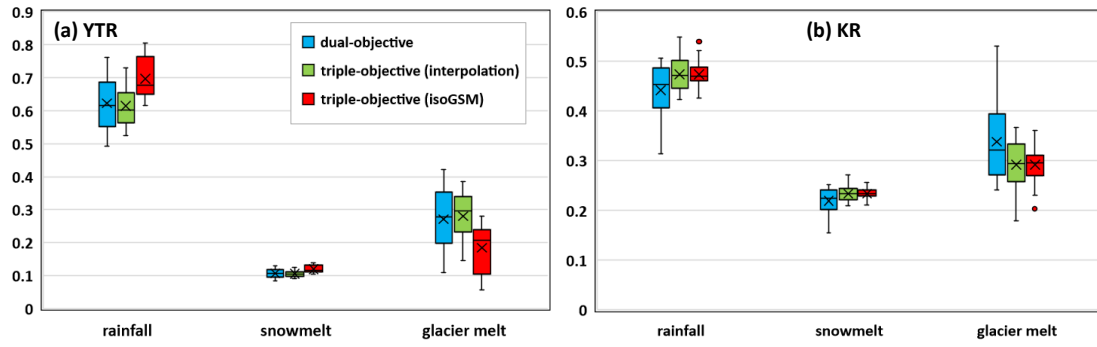
1014

1015

1016

1017

Figure 10. Uncertainty ranges of stream water $\delta^{18}\text{O}$ simulations in KR catchment during calibration and validation periods produced by the behavioral parameter sets of the dual-objective (a), [measurementinterpolation](#)-forced triple-objective (b), and isoGSM-forced triple-objective (c) calibration variants.



1018

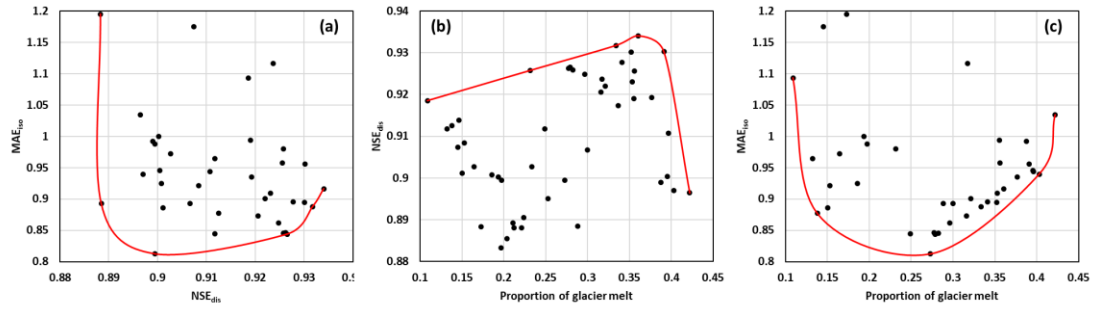
1019

1020

1021

1022

Figure 11. Average proportion and corresponding uncertainty ranges of different water sources in the annual water input for runoff generation estimated by different calibration variants in (a) YTR and (b) KR catchments.



1023

1024

Figure 12. The relationships between (a) MAE_{iso} and NSE_{dis}, (b) NSE_{dis} and glacier melt contribution and (c) MAE_{iso} and glacier melt contribution.

1025

1026

1027

1028

1029 **List of tables**

1030 **Table 1.** Characteristics of precipitation and stream water samples in YTR and KR
1031 catchments.

1032 **Table 2.** Calibrated parameters of the THREW-t model.

1033 **Table 3.** Comparisons of the model performance in YTR basin produced by different calibration
1034 variants.

1035 **Table 4.** Comparisons of the model performance in KR catchment produced by different
1036 calibration variants.

1037 **Table 5.** Average proportions of water sources in the annual and seasonal water inputs for
1038 runoff generation in YTR basin.

1039 **Table 6.** Average proportions of water sources in the annual and seasonal water inputs for
1040 runoff generation in KR catchment.

1041

1042

Table 1. Characteristics of precipitation and stream water samples in YTR and KR catchments.

Catchment (Station)	Year	Period Dd/mm to dd/mm	Precipitation sample number	Stream sample number
YTR (Nuxia)		14/03 to 23/10	86	34
YTR (Yangcun)	2005	17/03 to 05/10	59	30
YTR (Nugesha)		14/05 to 22/10	45	25
YTR (Lazi)		06/06 to 22/09	42	22
		2006	04/06 to 11/11	24
	2007	23/04 to 09/10	39	25
KR (Wengguo)	2010	05/05 to 18/10	63	23
	2011	28/03 to 06/11	69	32
	2012	16/06 to 22/09	42	14

1043

1044

Table 2. Calibrated parameters of the THREW-t model

Symbol	Unit	Physical descriptions	Range
nt	-	Manning roughness coefficient for hillslope	0-0.2
WM	cm	Tension water storage capacity, used in Xinanjiang model (Zhao, 1992) to calculate saturation area	0-10
B	-	Shape coefficient used in Xinanjiang model to calculate saturation area	0-1
KKA	-	Coefficient to calculate subsurface runoff in $Rg=KKD \cdot S \cdot K^S_S \cdot (y_s/Z)^{KKA}$, where S is the topographic slope, K^S_S is the saturated hydraulic conductivity, y_s is the depth of saturated groundwater, Z is the total soil depth	0-6
KKD	-	See description for KKA	0-0.5
T_0	°C	Temperature threshold above which snow and glacier melt	-5-5
DDF_N	mm/°C/day	Degree day factor for snow	0-10
DDF_G	mm/°C/day	Degree day factor for glacier	0-10
$C1$	-	Coefficient to calculate the runoff concentration process using Muskingum method: $O_2=C_1 \cdot I_1+C_2 \cdot I_2+C_3 \cdot O_1+C_4 \cdot Q_{lat}$, where I_1 and O_1 is the inflow and outflow at prior step, I_2 and O_2 is the inflow and outflow at current step, Q_{lat} is lateral flow of the river channel, $C_3=I-C_1-C_2$, $C_4=C_1+C_2$	0-1
$C2$	-	See description for $C1$	0-1

1045

1046 **Table 3.** Comparisons of the model performance in YTR basin produced by different calibration
 1047 variants.

calibration variant	behavioral ratio ^a	period /station ^b	NSE _{dis} ^{c,d}	RMSE _{SCA}	MAE _{iso}
Dual-objective	0.98	calibration	0.91 (0.86-0.93)	0.07 (0.07-0.10)	1.24 (0.90-1.99)
		validation	0.86 (0.77-0.92)	0.07 (0.06-0.09)	0.96 (0.75~1.97)
Triple-objective (measurement)	0.64	calibration	0.89 (0.85-0.92)	0.08 (0.07-0.10)	0.64 (0.47-0.86)
		validation	0.82 (0.75-0.89)	0.07 (0.07-0.09)	1.46 (1.17-1.93)
Triple-objective (isoGSM)	0.82	calibration	0.89 (0.85-0.93)	0.08 (0.07-0.10)	0.76 (0.70-0.84)
		validation	0.85 (0.76-0.91)	0.07 (0.07-0.09)	0.87 (0.76-1.04)

1048 a: Behavioral ratio represents the ratio of behavioral parameter set number to the run time of pySOT
 1049 program.

1050 b: “Period” for discharge and SCA simulation, and “station” for isotope simulation.

1051 c: Bracketed values represent the minimal and maximal values produced by the behavioral parameter
 1052 sets.

1053 [d: NSE_{dis} is calculated based on the simulated and observed streamflow at Nuxia station](#)

1054

1055 **Table 4.** Comparisons of the model performance in KR catchment produced by different
 1056 calibration variants.

calibration variant	behavioral ratio	period	NSE_{dis}	RMSE_{SCA}	MAE_{iso}
Dual-objective	0.78	calibration	0.79 (0.75-0.85)	0.10 (0.08-0.18)	2.18 (0.73-4.71)
		validation	0.80 (0.73-0.84)	0.08 (0.06-0.19)	2.38 (0.84-4.96)
Triple-objective (measurement)	0.13	calibration	0.74 (0.70-0.81)	0.13 (0.08-0.18)	0.68 (0.48-0.83)
		validation	0.79 (0.73-0.84)	0.11 (0.06-0.18)	0.93 (0.72-1.19)
Triple-objective (isoGSM)	0.12	calibration	0.74 (0.70-0.77)	0.12 (0.08-0.19)	0.69 (0.57-0.81)
		validation	0.79 (0.76-0.82)	0.10 (0.06-0.19)	0.77 (0.69-0.87)

1057

1058 **Table 5.** Average proportions of water sources in the annual and seasonal water inputs for
 1059 runoff generation in YTR basin.

Season	Water source ^a	Dual-objective	Triple-objective (measurement)	Triple-objective (isoGSM)
Annual	Rainfall	62.2	61.4	69.6
	Snow melt	10.7	10.6	12.0
	Glacier melt	27.1	28.0	18.4
	Uncertainty	11.4	8.6	8.9
Spring	Rainfall	35.4	36.8	44.2
	Snow melt	42.9	39.7	43.8
	Glacier melt	21.7	23.5	12.0
	Uncertainty	13.4	12.8	11.8
Summer	Rainfall	69.8	68.2	74.5
	Snow melt	3.4	4.4	6.4
	Glacier melt	26.8	27.4	19.1
	Uncertainty	10.2	7.9	8.7
Autumn	Rainfall	63.1	61.9	76.1
	Snow melt	3.5	3.5	2.7
	Glacier melt	33.5	34.7	22.0
	Uncertainty	16.1	12.8	13.3
Winter	Rainfall	11.9	12.8	30.8
	Snow melt	70.1	65.8	61.7
	Glacier melt	18.0	21.4	7.5
	Uncertainty	19.7	20.6	30.8

1060 a: The uncertainty of the contribution is defined as $E = \sqrt{E_R^2 + E_N^2 + E_G^2}$, where E_R , E_N and E_G
 1061 represent the standard deviations of the contributions of the water sources produced by the corresponding
 1062 behavioral parameter sets. Subscripts of R , N and G represent rainfall, snow meltwater and glacier
 1063 meltwater, respectively.

1064

1065 **Table 6.** Average proportions of water sources in the annual and seasonal water inputs for
 1066 runoff generation in KR catchment.

Season	Water source	Dual-objective	Triple-objective (measurement)	Triple-objective (isoGSM)
Annual	Rainfall	44.2	47.4	47.4
	Snow melt	22.0	23.4	23.4
	Glacier melt	33.8	29.2	29.2
	Uncertainty	9.4	6.2	4.7
Spring	Rainfall	4.1	4.5	4.5
	Snow melt	56.3	61.6	60.9
	Glacier melt	39.5	33.9	34.6
	Uncertainty	13.7	14.2	12.0
Summer	Rainfall	53.5	56.6	56.9
	Snow melt	14.0	15.2	15.1
	Glacier melt	32.4	28.2	28.0
	Uncertainty	9.7	5.1	3.9
Autumn	Rainfall	30.9	35.0	34.3
	Snow melt	33.9	35.3	35.5
	Glacier melt	35.1	29.7	30.3
	Uncertainty	11.2	11.0	9.6
Winter	Rainfall	0	0	0
	Snow melt	55.3	63.3	58.9
	Glacier melt	44.7	36.7	41.1
	Uncertainty	22.3	31.5	29.2

1067